University of Crete

Department of Materials Science and Technology

Master Thesis

Optical and Electronic Properties of few layers of GeSe

George Kourmoulakis

Supervisor: Prof George Kioseoglou

March 2018

CONTENTS

ACKNOWLEDGEMENTS

My special and sincere thanks to my supervisor Professor George Kioseoglou for giving me the opportunity to work with him, supporting me every step of the way taking time to provide me with his knowledge, his scientific experience and encouraging me fence with every research obstacle that I met during my master's program.

I would like to express my gratitude to Dr. Emmanuel Stratakis for his guidance and inspiration by providing ideas that helped my progress and giving me the space and time to work in his research lab under an amazing and professional work environment.

A very big heartily thanks belongs to my friend and colleague Dr. Ioannis Paradisanos for taking the time to help me every time I needed him, guiding me with his experience on the research subject that I chose to study and for being a true inspiration to me as a young scientist.

I am so grateful to the Institute of Electronic Structure and Laser (IESL) of the Foundation for Research and Technology-Hellas (FORTH) for the financial support, equipment and for making it possible for me to do research and study in my hometown.

Last, but not least, I owe many thanks to my family for supporting me, encouraging me to take my studies to a higher level and my friends that helped and believed in me.

ABSTRACT

Atomically thin two-dimensional (2D) materials including graphene have attracted significant research interest due to their extraordinary physical properties. However, graphene is a zero-band gap material which in some cases is an undesirable property for optoelectronic applications. Transition metal dichalcogenides (TMDs) and some IV-VI compounds combine the 2D layered structure with a finite gap and therefore are alternatives of graphene. Single layers of TMDs have a direct-gap at the K-point of the Brillouin zone with a range of bandgaps in the visible spectrum, making them suitable for optoelectronic applications from light emitting diodes to light harvesting and sensors. An indirect-to-direct-gap transition occurs at the monolayer limit resulting in strong excitonic photoluminescence (PL) emission. Remarkable electrical properties of these materials have also been demonstrated in field effect transistors and new phenomena have arisen in the family of TMDs.

In this thesis, we present a study of GeSe (IV-VI), a layered compound semiconductor that theoretical calculations reveal interesting electronic and optical properties. The predictions suggest that the crystal undergoes a direct to indirect energy bandgap transition at the limit of bilayer and monolayer. At the same time, the anisotropic spin splitting of the energy bands that comes from the interplay of spin-orbit coupling and lack of inversion symmetry renders this crystal optimal for spin related applications like spintronics. In addition, a monolayer of GeSe is found to be a strong absorber of visible light. We applied several exfoliation techniques with initial purpose to create a 2D layer of this crystal. However, GeSe is unstable in most of the situations we put it in and tends to change its phase in one or two phases of the more stable $GeSe_2$. This change of phase motivated us to find certain conditions under which we can cause intentionally this phase change.

Preamble

Layered materials that are build up by van der Waals forces can potentially reach the monolayer limit of thickness by various methods of exfoliation or Chemical Vapor Deposition (CVD) growth, while remaining in a stable state. These 2D materials attracted huge scientific interest because of their remarkable mechanical, optical and electronic properties which are absent in their three-dimensional (3D) counterparts. The application of strain, doping and external fields for example, can modify the material's properties in a very specific and controlled way **[1,2]**.

Graphene, a layer of carbon atoms arranged in a honeycomb lattice, is the most prominent example of these 2D materials. Its linear dispersion of energy yields to some unique electronic and optical properties **[3-5]**, however, at the same time, the lack of energy gap limits its applicability to devices that require high on/off current-ratio. Semiconductors come to play a complementary role in the field of 2D materials research with their unique optoelectronic properties and their highly versatile energy gap, which can be manipulated with various ways (like doping or application of an external electric field) depending on each application's demands **[1,2, 6-9]**.

GeSe crystal in bulk state, is an indirect bandgap semiconductor of the IV-VI family with an energy gap of 1.1 eV. The layers are stacked together in an orthorhombic lattice. The dimensions of a unit cell are a=4.38Å, b=3.82 Å and c=10.79 Å. Theoretical calculations predict a transition from indirect to direct bandgap at the bilayer and monolayer limit, a prediction that still needs an experimental verification. In addition to the predicted strong visible light absorbance, density functional and many-body perturbation theory indicate that the interplay of spin-orbit coupling and lack of inversion symmetry in the monolayers of GeSe structures results in anisotropic spin splitting of the energy bands, an optimal feature for directionally dependent spin transport applications **[10, 12]**.

The first section of this thesis is an introduction to GeSe crystal regarding its structure and optoelectronic properties **[10]**. Moreover, we'll give a detailed description of the experimental procedures we used for exfoliation and we'll close this first part discussing the theoretical background of Raman spectroscopy, our primary characterization technique, giving also details of the setup we used.

In the second part, we'll present our experimental results and demonstrate differences in morphology (color variations under an optical microscope) and Raman spectra correlating the exfoliation methods with the resulting phases of GeSe or $GeSe_2$ and comparing them with theory in order to verify and explain our findings.

In the last part, we farther discuss our results revisiting the purpose of our experimental work, stating our opinion over the outcome and suggesting different experimental approaches. It will be interesting to manipulate the conditions under which GeSe is exfoliated aiming to create a single-layer. For example, cooling the crystal down in a solution and applying stirring might have similar results with liquid phase exfoliation technique (for which powder is commonly used). Another idea is to perform laser thinning at very low temperatures or apply different values of pressure and investigate its behavior in ambient conditions.

I. Introduction

Materials in reduced dimensions often exhibit fundamentally new physics and phenomena that can potentially lead to novel applications. The transition metal dichalcogenides (TMDs), MX_2 (M = Mo, W and X = S, Se), which are weakly bonded layered structures that can be reduced to single layer two-dimensional (2D) semiconductor crystals, provide a good example. Unlike their three-dimensional (3D) counterparts that are indirect gap semiconductors, and unlike graphene which has a zero bandgap, single layers of MX_2 have a direct-gap at the K-point of the Brillouin zone with a range of bandgaps in the visible spectrum, making them suitable for optoelectronic applications from light emitting diodes to light harvesting and sensors **[6, 13-17]**. An indirect-to-direct-gap transition occurs at the monolayer limit resulting in strong excitonic photoluminescence (PL) emission **[18]**. Remarkable electrical properties of these materials have also been demonstrated in field effect transistors **[19]** and new phenomena have arisen in the family of TMDs.

TMD monolayers have a strong optical absorbance in the visible range and can be used to fabricate solar cells with light to electricity conversion efficiencies of ~0.5% **[19]**. Theoretical calculations also predict that the extraordinary absorbance of TMDs enables ultrathin (~1 nm) solar cells based on a stack of graphene and MoS2 with an energy conversion efficiency of up to 1% **[16]**. In addition to their unusual optical properties, atomically thin TMDs, display interesting spin physics that is promising for spin-transport applications. For example, the combined effects of spin−orbit coupling and inversion symmetry breaking in TMD monolayers results in a strong coupling of the spin and valley degrees of freedom that can be combined in spintronic and valleytronic devices. Like TMDs, several IV−VI compounds including GeSe and SnSe also crystallize in layered structures with weak bonding between the layers. SnSe was recently demonstrated to be an exceptionally promising thermoelectric material with a record figure of

merit at high temperatures [20, 21]. While atomically thin TMD compounds have been the subject of extensive research, little is known about the properties of few-layer IV−VI materials. Tritsaris et al. studied few-layer SnS and found its optoelectronic properties to be tunable with the number of layers [22]. In addition, density functional theory (DFT) calculations show that single-layer IV−VI compounds are stable in either a distorted NaCl or litharge structure with formation energies comparable to single-layer MoS_2 [23], which indicates that mechanical exfoliation of bulk IV−VI materials may also be a possible route to produce atomically thin samples.

Bulk GeSe is an indirect band gap semiconductor with energy of 1.1eV and DFT calculations predict a transition to direct gap at the two- and one-layer limit. The interplay of spin−orbit coupling with the symmetry of the monolayer structures results in anisotropic spin-orbit splitting of the bands that can find applications in directionally dependent spin-transport devices. In addition, the optical absorbance in the visible range is high for the few-layer GeSe structures, reaching values as high as 47% for bilayer GeSe with a thickness of just 1 nm. All these imply that GeSe are promising materials for ultrathin-film flexible photovoltaic applications with an upper limit to the conversion efficiency that rivals the record efficiencies of organic and dye sensitized solar cells.

1. Germanium Selenide

1.1 Crystal Structure of GeSe

Germanium Selenide belongs to orthorhombic space group D^{16}_{2h} (Pnma) and is closely related to the black phosphorous structure. Its lattice parameters are a=4.388A, b=3.833A and c=10.825A and correspond to the Γ-X, Γ-Y, and Γ-Z directions in the first Brillouin zone respectively **(Fig.1)**

[24]. The unit cell contains eight atoms organized in two adjacent double layers as shown in Fig.1a. The atoms in a single layer are joined to three nearest neighbors by covalent bonds which form zigzag chains along the b-axis. All GeSe crystal cleave easily in the a-b plane since van der Walls bonding predominates along the c-axis. The anisotropy crystal structure implies that significant differences are to be expected among the optical spectra with an electric vector parallel to the a, b, and c directions. [10, 11, 25-27].

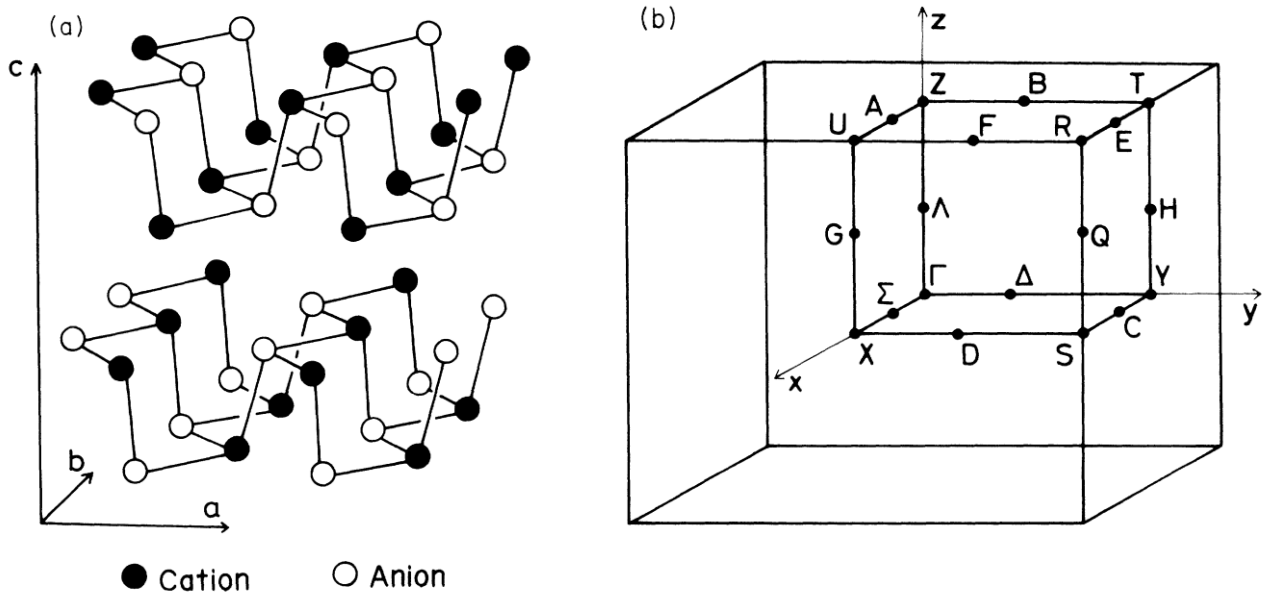

***Figure 1.1**: a) GeSe crystal structure. The unit cell is defined by a, b, c, axes where a>b and c is perpendicular to the cleavage plane. b) Brillouin zone of the crystal. The x,y, z directions correspond to the b ,a, and c crystallographic axes.*

1.2 Electronic Structure of GeSe

Bulk GeSe is an indirect bandgap semiconductor. The energy gap of 1.10 eV is calculated based on Density Functional Theory (DFT) and many-body perturbation and it's in a good agreement with optical-absorption measurements (1.10 eV). Calculations predict two local conduction-band minima, one is located along the Γ-X direction and the other one along Γ-Y direction, while the valence-band maximum is located along Γ-Y (Fig.1.2). When GeSe crystal reaches the double-layer and single-layer limit, it becomes a direct-bandgap semiconductor (the conduction-band minimum and the valence-band maximum are at the same K-point of the Brillouin zone). The monolayer is predicted to have an energy bandgap of 1.87eV while the bandgap of the bilayer is predicted to be 1.72 eV. However, the difference of 20-30 meV between direct and indirect transition lays within the calculation's typical error (0.1 eV) and thus, there is a possibility that the computational methods did not gave accurate results for the electronic band structure. The latter, is not unexpected since DFT underestimates the band-gap of materials due to unreliable calculations over the excited states. In addition, the strong exciton binding energy for few-layer GeSe materials (0.32eV for one-layer and 0.23eV for two-layers) that results from weak screening compared to bulk cases in low-dimensional systems, may affect the band-gap **[10, 28, 29]**.

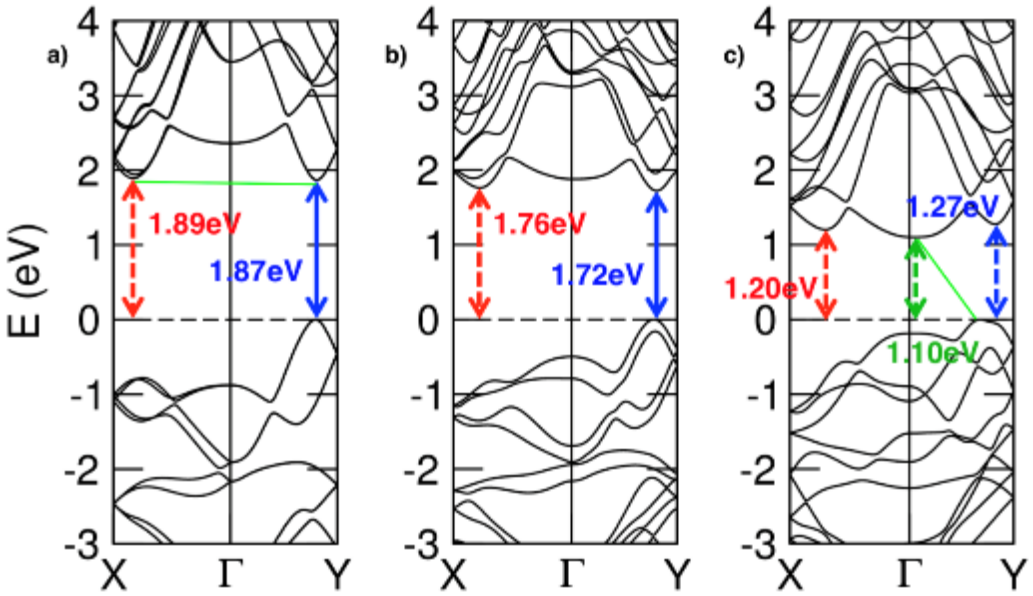

Figure 1.2: a) transition energies in single-layer GeSe. b) transition energies in double-layer GeSe. c) transition energies in bulk GeSe. The dashed arrows indicate indirect transitions while the solid arrows indicate direct. The minimum gap for single and double-layer is located along the Γ-Y direction. The small energy difference (for single and double-layer) between direct and indirect transition is clearly shown in this figure. **[10]**

The small energy difference referred to conduction-band minimum along Γ-X and Γ-Y allows for tunability between direct and indirect phase of the semiconductor by simply applying external controls like strain. The lack of inversion symmetry for single-layer GeSe leads to broken band-spin degeneracy (except for points along Γ-Y) by spin-orbit coupling. This anisotropic splitting of the bands may find use in applications for directionally dependent spin transport.

1.3 Optical properties of GeSe

GeSe shows a p-type semiconducting character with indirect bandgap of 1.1eV. The value of thermoelectric power for the bulk is 1mV/K at T=273K for the single crystal and carrier concentration ranging from $7x10^{16}$ to $5x10^{17}/cm^3$. The optical absorption coefficient reaches 10^4 cm^{-1} in infrared region. The photoconductive spectral response shows the activation energy to be around 1.5 eV for the main band and 1.17 eV for the secondary band, values that are close to the energy gaps **[30]**.

Theoretical calculations over the absorption of GeSe crystal triggered the interest of scientific community since few-layer structures of GeSe are predicted to be strong absorbers in the visible range. The differentiation in absorption spectra with respect to direction of polarized light is directly related to the in-plane anisotropy of the crystal. Scaling down to thinner structures of GeSe, there is a blueshift for both the direct band-gap and the optical gap. For few-layer structures, quantum confinement and strong interactions between electrons result in bandgap enhancement. This phenomenon combined with the increased exciton binding energy resulting from the overlapping of electron-hole wave functions, determine the quantitative control of blueshift. In Fig.1.3, optical absorption spectra are shown as a function of photon energy and polarization. Absorbance A is calculated according to:

$$A = 1 - e^{-a(E)d} = 1 - e^{-\frac{2\pi E d \varepsilon_2}{hc}}$$

where E is the photon energy, α is the absorption coefficient, ε_2 is the imaginary part of dielectric function and d is the thickness of simulation cell perpendicular to the layers **[10, 31]**.

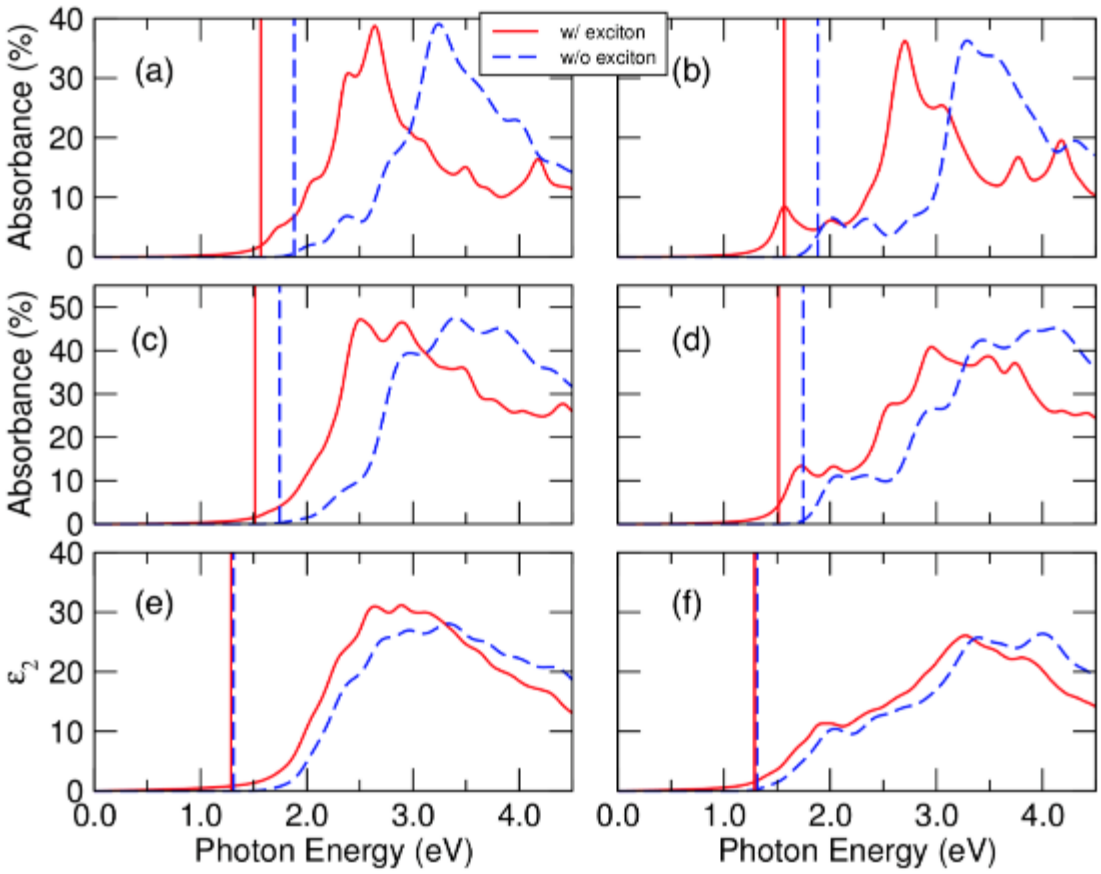

Figure 1.3: (a, b) optical absorption spectra for monolayer GeSe, (c, d) double-layer GeSe, (e, f) bulk GeSe. Light is polarized along zig-zag direction for graphs on the left side and armchair direction for graphs on the right side. Solid red lines represent spectra with excitonic effects and blue dashed lines represent spectra without excitonic effects. The vertical lines indicate the initiation of optical absorption. **[10]**

The visible-light absorbance of the few-layer materials is found to be remarkably large, approaching values up to 38% percent in single-layer and 47% percent in double-layer GeSe. This high absorbance in the few-layer structures is attributed to the nature of the atomic orbitals that form the band extrema of these materials. Since the group-IV cations occur in the 2+ charge state,

the lowest conduction bands consist of cation p orbitals (Ge 4p), while the filled Se valence 4p orbitals form the topmost valence bands. Since there are three p orbitals per cation that are directional in space, they give rise to three anisotropic bands per cation atom in the unit cell, each with large effective mass along the directions perpendicular to the p orbital orientation axis. The band character in GeSe is in contrast to direct-gap III−V semiconductors such as GaAs, for which the s-orbital character of the conduction-band minimum at Γ results in a unique, isotropic conduction band with a small electron effective mass. Because of the larger number of bands that occur near the band extrema and their larger directionally averaged effective masses, the joint density of states is larger in GeSe than in III−V compounds and results in a larger probability of optical transitions across the gap and therefore a larger absorption coefficient.

2. Absorption and Raman Spectroscopy

2.1 Absorption

Absorption spectroscopy is a term describing any spectroscopic technique that measures the absorption of electromagnetic radiation due to its interaction with matter. During an absorption experiment, photons of selected frequencies are directed onto the sample and relative transmission of the various photons is observed. Figure 2.1 shows a simplified energy diagram of two separate bands in a semiconductor. There are two requirements for transitions of electrons between the valence and the conduction band and vice versa: (a) the energy has to be conserved and (b) the momentum has to be conserved. The law of conservation of energy applied to the interband transition dictates that:

$$Ef = Ei + h \cdot f \qquad (2.12)$$

where Ei and Ef is the electron energy in the valence and conduction band, respectively and h·f is the photon energy. It is apparent from Fig. 2.10 that the minimum value of (Ef – Ei) is equal to Eg. This signals that the absorption exhibits a threshold behavior: the energy of a photon can be transferred to an electron in the valence band and excite it to the conduction band, if the photon energy is larger than the bandgap energy Eg. The photon is absorbed during this process and an electron–hole pair is generated. As the photon energy is reduced below Eg, the crystal becomes transparent to light. Additionally, the existence of a continuous range of energy states within the upper and lower bands implies that the interband transitions will be possible over a continuous range of frequencies, contrary to isolated atoms which exhibit discrete absorption lines.

Conservation of momentum demands that the change in crystal momentum of the electron must equal the momentum of the photon. Due to the negligible photon momentum, this restriction practically requires that the electron wave vector does not change significantly during the absorption process:

$$k_f \approx k_i \tag{2.13}$$

ki, kf are the wavevectors of the initial and final electron state. Therefore, photon absorption is represented as a vertical line on E-k diagrams. It is apparent that this second restriction strongly correlates with the bandgap nature of the material. For a direct-gap semiconductor, the fact that the minimum of the conduction band is above the maximum of the valence band readily satisfies Eq. (2.13). On the other hand, band extrema do not coincide in indirect-gap materials. As a result, a phonon is needed for the conservation of the momentum to enable the interband transition of an

electron from the maximum of the valence band to the minimum of the conduction band. Indirect transitions are characterized as second-order processes as they require three entities to intersect in order to proceed: an electron, a photon and a phonon. Direct interband transition are instead first-order processes since there is no phonon participation. Subsequently, the two-particle process is less probable and has a much smaller transition rate. However, indirect absorption plays a crucial role in technologically important devices such as silicon detectors and solar cells **[32]**.

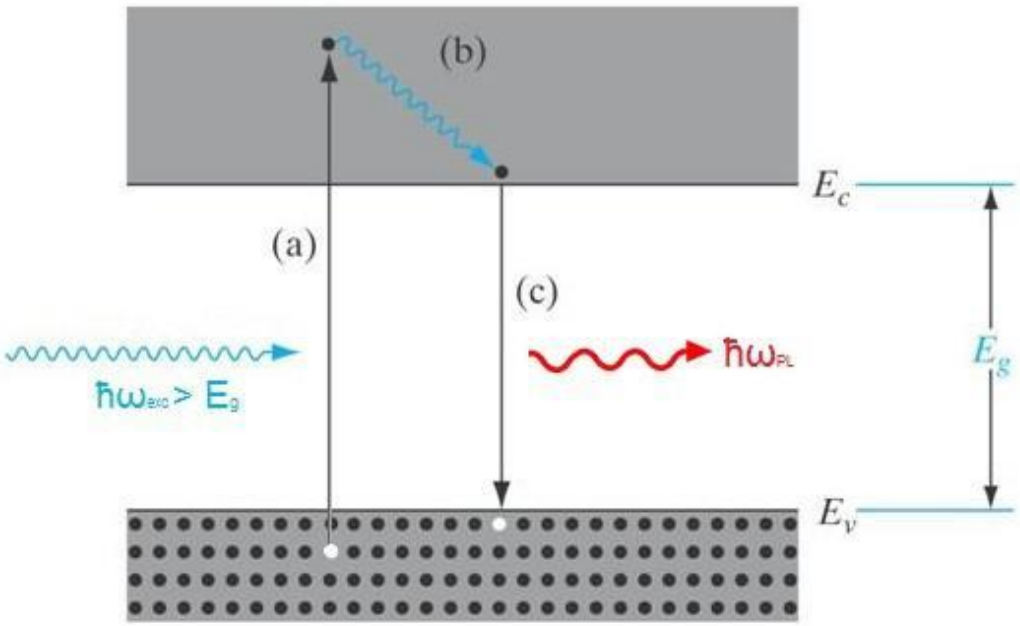

Figure 2.1: Simplified energy diagram illustrating the (a) absorption of a photon with energy greater than the energy gap, (b) thermalization of the electron and (c) re-emission of a photon with energy lower than the absorbed photon. ***[32]***

2.2 Raman Spectroscopy

Vibrational spectroscopic methods constitute a powerful tool in analyzing some of the most fundamental processes in physical chemistry: molecular vibrations. These methods measure vibrational energy levels which are associated with chemical bonds and provide information about the molecular composition, structure and interactions within the sample. Vibrational spectroscopy can be used for a wide range of applications in material characterization such as sample identification and quantification, crystal structure and quality determination, reaction monitoring etc. While there are various experimental techniques used to analyze those vibrations, most are variations of Raman and Infrared (IR) spectroscopy.

When light interacts with matter, the photons which make up the light may be reflected, absorbed, transmitted or scattered. Scattering is the phenomenon in which light changes direction and possibly also its frequency after interacting with the studied medium. The scattered radiation is elastic if its frequency remains unchanged or inelastic if the frequency changes in the process. The basic principle behind Raman spectroscopy is the detection and analysis of inelastically scattered light from the medium, produced by the interaction of light with the atomic or molecular vibrations. Inelastic scattering was first observed in molecules by C.V. Raman and K.S. Krishnan in 1930 **[33]** and since then it has been proven as a useful tool in probing the fundamental excitations in matter.

According to classical theory **[34]** Raman scattering can be explained as follows: The electric field strength (E) of the electromagnetic wave (usually a laser beam) oscillates with time (t) as shown by Eq. (2.1):

$$\mathbf{E = E_0 \cdot \cos(2\pi \cdot \nu_0 \cdot t)} \qquad \mathbf{(2.1)}$$

where E_o is the electric filed amplitude and ν_o is the laser frequency. When a molecule is irradiated by this light, a subsequent electric dipole moment p is induced which is directly proportional to the electric field:

$$\mathbf{p} = \boldsymbol{\alpha} \cdot \mathbf{E} \qquad \textbf{(2.2)}$$

The proportionality constant α is called polarizability of the molecule and describes how easily the molecule can be deformed i.e. the tendency of its charged distribution to be displaced by the external electric field. It highly depends on the shape and dimensions of the chemical bonds and in the general case, is a tensor because molecules tend to polarize more readily in some directions than others. Given the fact that chemical bonds change during vibrations, the polarizability is dependent on molecular vibrations. In other words, it depends on the normal coordinate Q of the molecule:

$$\boldsymbol{Q = Q_0 \cos(2\pi \nu_{vib} t + \varphi) = Q_0 \cos(2\pi \nu t + \varphi)} \qquad \textbf{(2.3)}$$

Here, Q_o and ν are the vibrational amplitude and frequency, respectively, and φ is a phase angle. For a small amplitude of vibration, α is a linear function of Q. Thus, we can write:

$$\boldsymbol{a = a_0 + \sum_k \left(\frac{\partial a}{\partial Q_k}\right)_{Q0} Q_k + \frac{1}{2}\sum_{k,l}\left(\frac{\partial^2 a}{\partial Q_k \partial Q_l}\right)_{Q0} Q_k Q_l + \ldots\ldots} \qquad \textbf{(2.4)}$$

where, αo is the polarizability at the equilibrium position and Qk and Ql are the normal coordinates that correspond with the kth and lth normal vibrations with frequencies fk and fl. In a first approximation, only the first two terms will play a significant role. Therefore, considering the vth normal vibration, Equation (2.4) is modified to:

$$a = a_0 + \sum_k \left(\frac{\partial a}{\partial Q_k}\right)_{Q0} Q_k = \alpha_0 + \alpha_\nu'.\ Q_\nu \qquad (2.5)$$

Substitution of Equation (2.3) to (2.5) yields:

$$a = \alpha_0 + \alpha_\nu'.\ Q_\nu = a_0 + \alpha_\nu'\ .Q_0\ cos(2\pi\,\nu\,t + \varphi) = a_0 + \beta\ cos(2\pi\,\nu\,t + \varphi) \qquad (2.6)$$

Where

$$\beta = \alpha_\nu'.\ Q_0 = \frac{\partial a}{\partial Q} Q_0$$

By combining (2.1) and (2.6) with (2.2), we obtain:

$$p = [a_0 + \beta\ cos(2\pi\,\nu\,t + \varphi)]E_0 cos(2\pi\nu_0 t) =$$

$$= a_0 E_0 cos(2\pi\nu_0 t) + \beta\ E_0 cos(2\pi\,\nu\,t + \varphi) cos(2\pi\nu_0 t) =$$

$$= a_0 E_0 cos(2\pi\nu_0 t) + \frac{1}{2}\beta E_0 \cos[2\pi(\nu_0 + \nu)\,t + \varphi] + \frac{1}{2}\beta E_0 \cos[2\pi(\nu_0 - \nu)\,t - \varphi] \qquad (2.7)$$

Therefore, the induced dipole moment consists of three terms. For clarity, the above equation is rewritten as a function of frequencies νo and ν:

$$\mathbf{p = p_1(\nu_0) + p_2(\nu_0 - \nu) + p_3(\nu_0 + \nu)}$$

The first term represents the case of elastic scattering, where an oscillating dipole radiates light of frequency equal to that of the external electromagnetic radiation, νo. This type of elastic scattering is called Rayleigh scattering and does not involve any energy change between the incoming and scattered radiation. The last two terms describe the inelastic or alternatively called Raman scattering. The second term corresponds to the so-called Stokes scattering where the frequency is reduced by a factor of ν, implying that the scattered photon has lost energy to the molecule. In contrast, during an Anti-Stokes process the photon has gained energy (νo + ν). If (∂α/∂Q)o is zero then β=0 and therefore

p = p1(vo) and all the scattered radiation originates from elastic processes. In that case, the vibration is said to be Raman-Inactive. To be Raman-active, the rate of change of polarizability with the vibration must be different than zero.

Now that Raman effect has been derived using the classical theory, we can use the quantum theory to better visualize the process and determine additional information (See Fig. 2.1) **[35].** According to the quantum interpretation, radiation is emitted or absorbed because of a system making a downward or upward transition between two discrete energy levels. When light is incident on our system, a short-lived state called a virtual state is formed in which the molecule is being excited. This state is not stable, and the photon is quickly re-radiated. When this occurs, there are three potential outcomes. Firstly, the molecule can relax back to its ground electronic state and emit a photon of equal energy to that of the incident photon (Rayleigh scattering). Secondly, the molecule can relax to a real vibrational state and emit a photon with less energy than the incident photon (Stokes scattering). The third possible outcome is that the molecule is already in an excited vibrational state, is excited to a higher virtual state, and then relaxes back down to the ground state emitting a photon with more energy than the incident photon (Anti-Stokes scattering). In the last

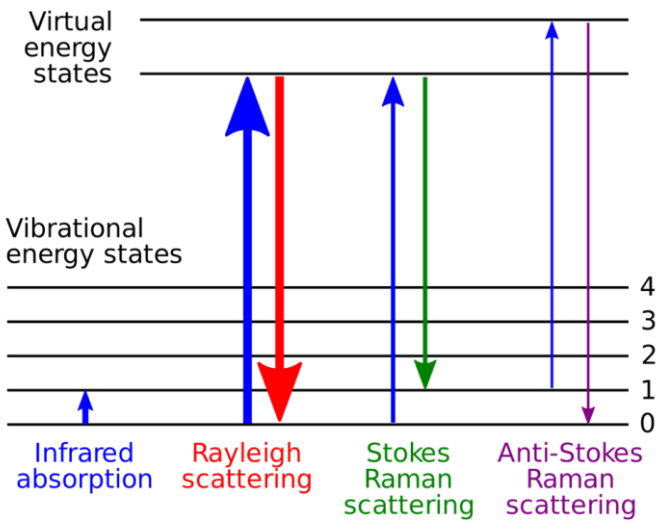

Figure 2.2: Schematic diagram representing transitions for Rayleigh and Raman Scattering.

two cases, the scattered radiation is what we measure experimentally as Raman scattering and the energy difference between the excitation and scattering process corresponds to the energy of vibrations of the molecule. Raman scattering is inherently a weak process as only a small fraction of light (approximately 1 in 10^7photons) is inelastically scattered.

The intensity of Raman peaks is given by

$$I = K\, a^2 P \frac{1}{\lambda^4}$$

where K is a proportionality constant, α is the polarizability, P is the laser power and λ is the wavelength of incident photons. Therefore, only the last two parameters are under the control of the spectroscopist, who can tune them to constitute Raman scattering as a non-negligible scattering mechanism.

A typical Raman spectrum illustrates the intensity of the scattered light as a function of its frequency or, more commonly, wavenumber difference to the incident radiation. Peaks corresponding to Stokes and Anti-Stokes processes appear symmetrically around the laser line, but the relative intensities depend on the initial population of the various states of the molecule which in turn depends on temperature. According to Maxwell–Boltzmann statistics, the lower state will be more populated than the upper state in thermodynamic equilibrium. Consequently, most molecules will be found in the ground state at room temperature, thus anti-Stokes scattering will be substantially weaker than the Stokes Raman scattering. Most Raman measurements are performed considering only the Stokes shifted light.

In this section so far, Raman scattering has been described in terms of the first-order contribution, in which only one vibrational unit is emitted or absorbed. In solids, normal vibration modes are quantized by quasiparticles called phonons. Under the restriction of momentum conservation, this process involves only phonons with wavevector $q \approx 0$ (i.e. the center of the Brillouin zone) due to the negligible momentum of light. In contrast, second-order Raman processes include features coming from different crystalline momenta, potentially from the entire Brillouin zone. For two different phonons with frequencies fa and fb and wavevectors qa and qb, peaks with Raman frequencies $\nu a + \nu b$ and $\nu a - \nu b$ are referred to as the combination and difference modes, respectively. Wavevector conservation in two-phonon Raman scattering is satisfied when $qa \pm qb \approx 0$. If the two phonons are identical, the resultant two-phonon Raman peak is known as an overtone. In overtone scattering the condition implies $qa = - qb$, i.e. the two phonons have equal and opposite wavevectors. Thus, in two-phonon Raman scattering there is no restriction on the magnitudes of the individual phonon wavevectors as there is in one-phonon scattering (only their sum must be near zero). Second-order Raman scattering is usually much weaker than first-order scattering but can be

enhanced by various mechanisms **[36].** When the energy of the incoming light coincides with an electronic transition, the system is excited not to a virtual but an electronic state and the absolute Raman intensities can be enhanced by several orders of magnitude. This variation is called Resonance Raman **[34].**

Infrared spectroscopy also measures the vibrational energies of molecules. The basic principle behind IR spectroscopy is the measurement of absorption of infrared light by the sample as a function of frequency. In particular, infrared energy covering a range of frequencies is directed onto the sample. Absorption occurs where the frequency of the incident radiation matches that of a vibration so that the molecule is promoted to a vibrational excited state. The loss of this frequency of radiation from the beam after it passes through the sample is then detected.

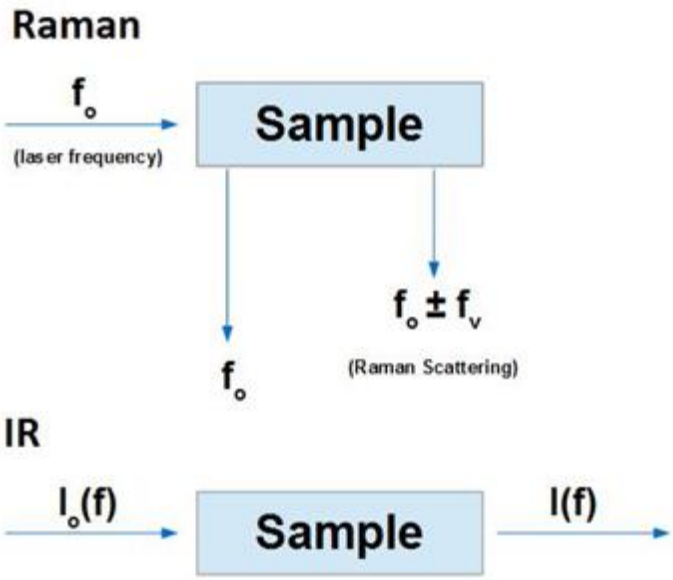

Figure 2.3: Illustration of Raman and IR vibrational spectroscopies. In the bottom figure, Io and I denote the intensities of the incident and transmitted beams, respectively

The main difference between the two spectroscopic methods is manifested in the different selection rules applying to each one. As previously mentioned, for a vibration to be Raman active there must be a change in the polarizability of the molecule during this vibration. On the other hand, an IR transition is detected when the molecule undergoes a dipole moment change during the vibration. For instance, when studying symmetrical molecules, e.g. O2, we cannot observe any IR lines as the molecule is unable to change its dipole moment. Another difference can be found in the excitation source. Modern Raman spectroscopy uses a monochromatic laser beam in the visible, near-infrared, or near ultraviolet region of the electromagnetic spectrum. This is not the case for IR spectroscopy where a laser beam is used in the infrared regime. The wavelength is changed over time, thus allowing the observation of all the absorption lines within the studied range of the infrared region. Unlike infrared absorption, Raman scattering does not require matching of the incident radiation to the energy difference between the ground and excited electronic states.

2.3 Raman spectroscopy of Germanium Selenide

Raman spectroscopy is an important tool for characterizing layered materials since it can provide information on the crystal structure, electronic structure, lattice vibrations and flake thickness while at the same time it can be used to probe strain, stability, charge transfer and layer orders. As we mention in section 1.1, bulk GeSe has an orthorhombic crystal structure. The unit cell contains eight atoms organized in two adjacent double layers. It can be viewed as a distorted rocksalt structure forming double-layer planes along c (c= 10.825 Å, b= 3.833 Å, a= 4.388 Å) which corresponds to z axis **[37]**.

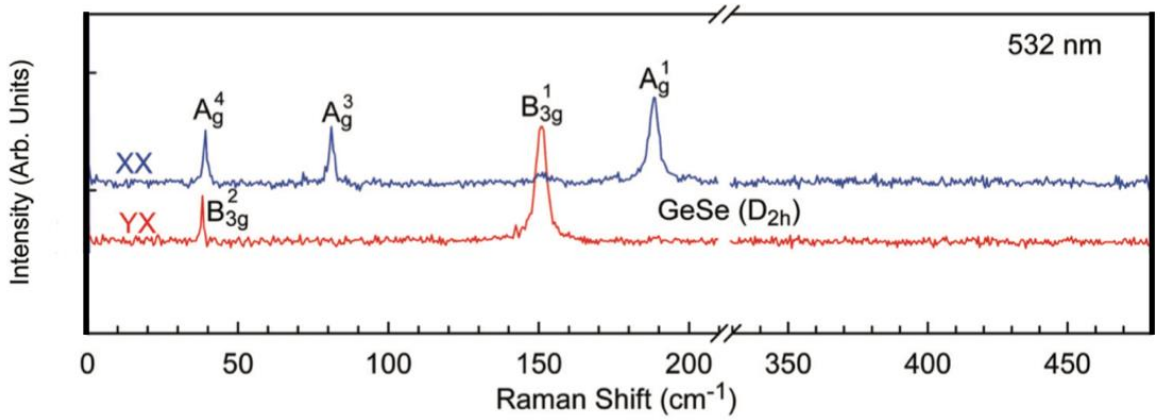

Figure 2.4: Raman spectra of bulk GeSe crystal under XX (unpolarized) and YX polarized configuration ***[37].***

The modes observed under XX polarized configuration **[37]** were 40 cm^{-1} assigned as A_g^4, 82cm^{-1} assigned as A_g^3 and 188cm^{-1} assigned as A_g^1 while under YX polarized configuration the modes observed were 39cm^{-1} assigned as B_{3g}^2 and 151cm^{-1} assigned as B_{3g}^1 (Fig. 2.4). The low-lying Raman active phonon frequencies can be identified as rigid-layer modes. The A_g^3 and B_{3g}^2 were identified as the interlayer shear modes within the *bc* plane. Another mode observed using different excitation wavelength (633nm) was the one at 175cm^{-1} assigned as A_g^2. Additional reports reveal all the active

modes of GeSe regarding different symmetries. Thus, in B_{1g} symmetry there are two modes (78cm^{-1} and 166cm^{-1}) and in B_{2g} symmetry the modes observed are 70cm^{-1}, 102 cm^{-1}, 199 cm^{-1} and 226 cm^{-1} **[38-40].**

In our Raman setup, we can't observe any vibrational mode below 100 cm^{-1} because of the notch filters used. Therefore, we can only monitor the strong modes B^1_{3g} (at 150 cm^{-1}) and A^1_g (at 188 cm^{-1}) as well as the weaker A^2_g mode at 175 cm^{-1}. Figure 2.5 shows the movement of the Ge and Se atoms for these three modes.

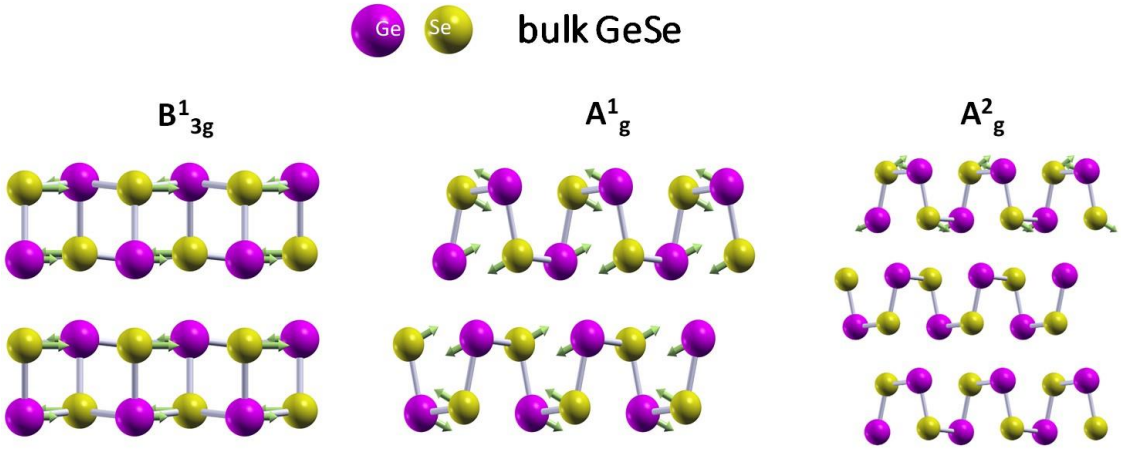

Fig.2.5: The three main vibrational modes of bulk GeSe. B^1_{3g} at 150 cm^{-1}, A^1_g at 188 cm^{-1} and A^2_g mode at 175 cm^{-1}.

Regarding the fact that the goal is to reach the bilayer or the monolayer limit where the indirect-to-direct gap transition is predicted to occur, there are calculations studying the behavior of Raman modes with respect to the number of layers (Fig.2.6, private communication with Prof E. Kioupakis). The calculations revealed a red shift upon reducing the number of GeSe layers.

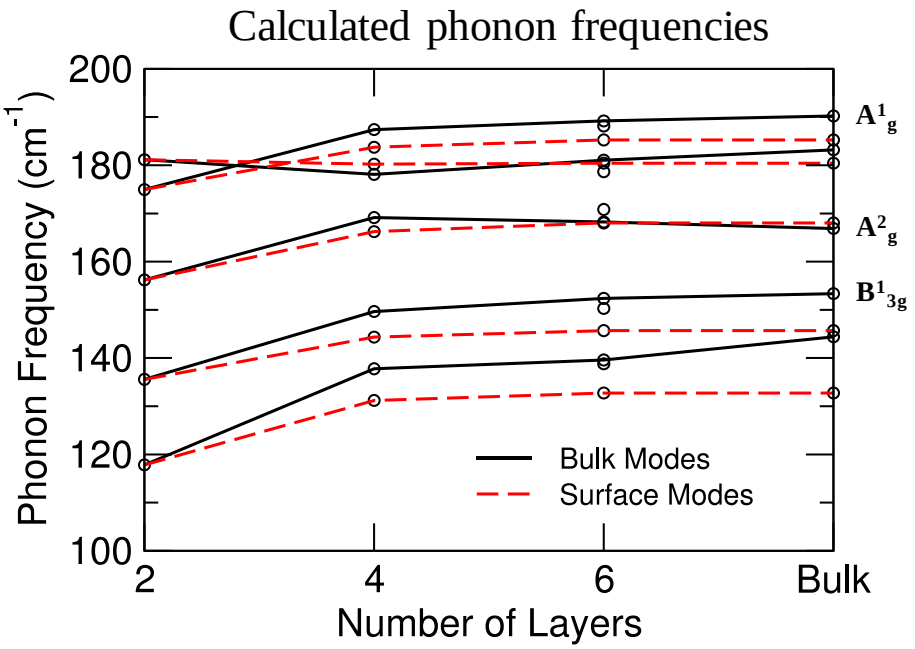

Figure 2.6. Calculated GeSe phonon frequencies as a function of the number of layers (courtesy of Prof E. Kioupakis)

3. Experimental Methods

3.1 Raman Spectrometer

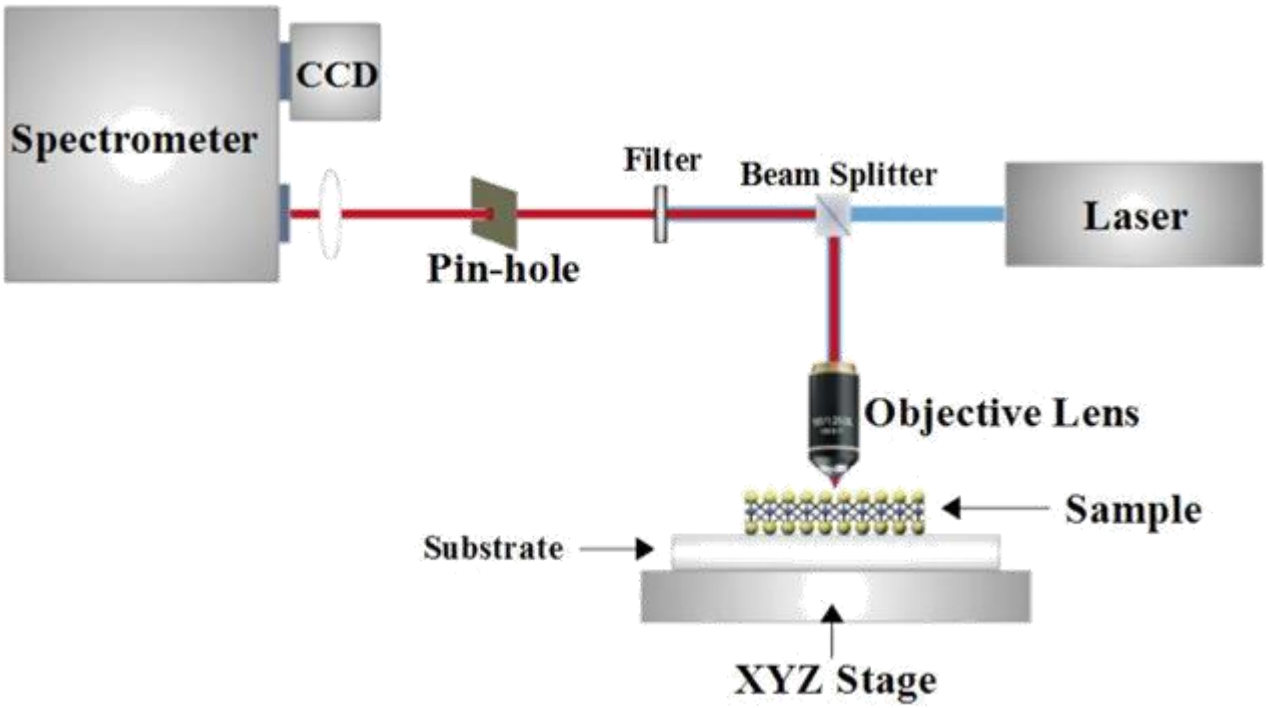

Figure 3.1: Schematic illustration of a confocal micro-Raman Spectrometer.

Modern micro-Raman (μ-Raman) instrumentation is based on three primary components: a laser as the excitation source, a spectrometer as the detector and a microscope as a sampling apparatus. By coupling a visible spectrometer to a microscope, Raman analysis with a laser spot of the order of 1 to 2 μm is achieved. However, simply adding a microscope assists in giving lateral (XY axes) spatial resolution but does not give depth (Z axis) spatial resolution. For this purpose, confocal optics are required.

Figure 3.1 schematically depicts a generic confocal Raman setup. The laser beam passes through a beam splitter and then is focused onto the sample by an objective lens. Scattered radiation is collected from the microscope through the objective and hits the beam splitter which now acts as a mirror. A filter is placed to remove the much more intense Rayleigh scattering which could potentially damage the light detector. If only Stokes (anti-Stokes) scattering is to be measured, a long (short) pass filter with a sharp edge close to the wavelength of the laser can be used. If instead we wish to measure both the Stokes and anti-Stokes radiation, a notch filter should be employed to block only a narrow band about the laser wavelength. After the filter, the radiation is arranged to pass through a pinhole aperture (25 to 100 μm in diameter) which rejects signals that are not in the focal plane of the objective. Consequently, the out-of-focus background (substrate) signals can be effectively reduced and it is possible to measure the Raman spectrum of a sample at different depth by moving the focal plane in the Z-direction. The in-focus scattered light enters a spectrometer where is being spectrally dispersed by a diffraction grating. Finally, the dispersed light is projected onto a Charged Coupled Device (CCD), a silicon-based semiconductor arranged as an array of photosensitive elements. The incoming photons are converted into an electrical signal which then is turned into a digital signal. The result is a spectrum with a number of counts assigned to each resolvable energy. The Raman scattering is collected in the so-called back-scattering geometry since the laser beam is focused onto the sample with an objective lens and the scattered light is collected with the same objective.

All the Raman spectra presented in this thesis have been measured by a Thermo Scientific, Nicolet Almega XR Micro Raman analysis system (Fig.3.2). It consists of a confocal single monochromator spectrometer which is interfaced with the microscope entirely using high-throughput, free-space optics. It is equipped with three microscopy objective lenses, a scanning motorized XYZ stage and two diode-pumped solid-state laser (DPSS) at 473nm and 780nm. The power of the incident beam is controlled with a neutral density filter and a high-resolution grating (2400 grooves/mm) analyzes the signal. A 100 μm pinhole is used as the confocal aperture. A 100x lens with a numerical aperture of 0.90 is used in all measurements, yielding a spot diameter of 0.5 μm **[41]**.

Fig.3.2: Nicolet Almega XR Micro Raman analysis system

3.2 Sample preparation - Exfoliation procedures

A critical factor when dealing with 2D materials is their observation and correct thickness identification. Few-layer materials are very thin and hard to identify under a microscope. Therefore, the selection of SiO_2/Si substrates is very important. The thickness of the SiO_2 determines the contrast with optimum values of 90 and 285 nm. The substrates were purchased from "Graphene Supermarket" company. They featured 100mm diameter, 700μm thickness, a polished surface to deposit the material of interest and a back etched surface. We purchased high quality GeSe crystals (3 to 5 mm in size) and ready to be exfoliated from "2D Semiconductors" company.

3.2.1 Mechanical exfoliation

This is the most common, easy and fast exfoliation technique to create few-layer samples of materials for research. The only drawback of this experimental procedure is the fact that it is not controllable meaning that no matter the crystal of interest, it can't guarantee single or double-layer flakes every time it is used **[42]**. The experimental procedure is described by the following steps. At first, we isolate a small part of bulk GeSe crystal, we cut a part of SiO_2 substrate and we also obtain a typical scotch-tape piece (Fig. 3.3).

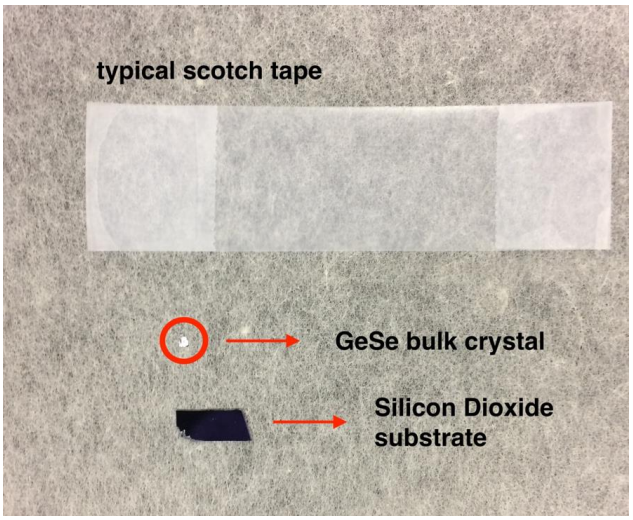

Figure 3.3: a piece of scotch-tape, a small bulk part of GeSe crystal and a part of SiO_2 substrate are the components we need for scotch-tape exfoliation

We place the bulk GeSe flake on the sticky side of the scotch-tape (Fig.3.4), preferably not in the middle, and then we repeatedly stick and unstick together the surface of scotch-tape to create a spread of exfoliated material.

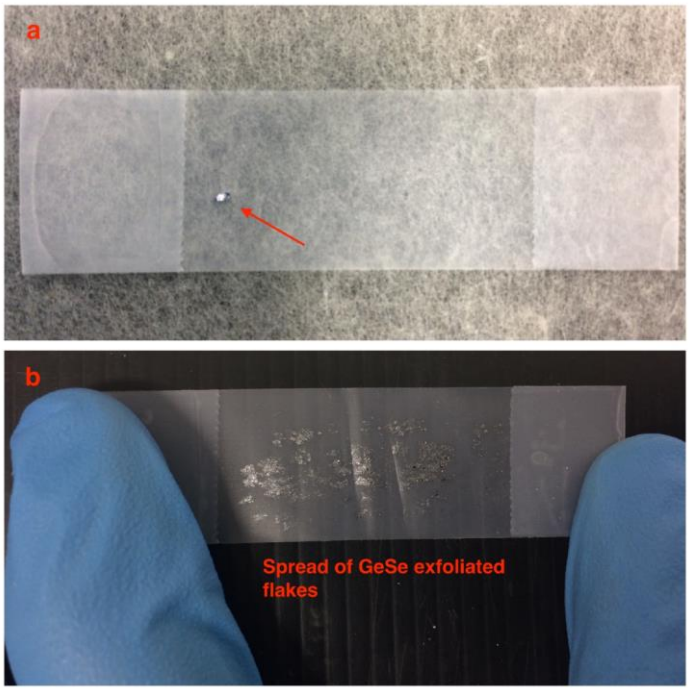

Figure 3.4: a) Bulk GeSe flake placed on the sticky side of scotch-tape. b) Spread of GeSe flakes created by multiple exfoliations on the same scotch-tape.

For the second step, we place the substrate on top of the exfoliated flakes using its polished surface. This way we aim at getting on the substrate thin pieces from bulk exfoliated flakes taking advantage of surface-material interactions.

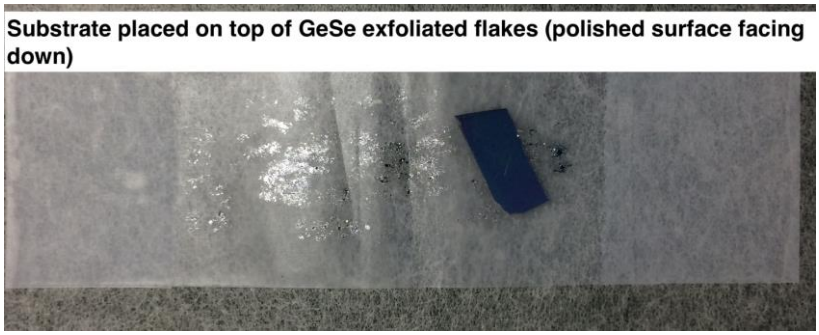

Figure 3.5: Substrate stack on the scotch-tape containing exfoliated GeSe flakes. We preferably select an area with denser spread of material increasing our chances of getting a thin flake

Next, we apply pressure on the non-sticky side of the scotch-tape just under the substrate to force more material to move from the upper parts of GeSe flakes to the SiO_2 substrate. Slowly but steady, we peal the substrate off the scotch-tape taking our time in order to get as much material as we can and as little amount of glue as possible.

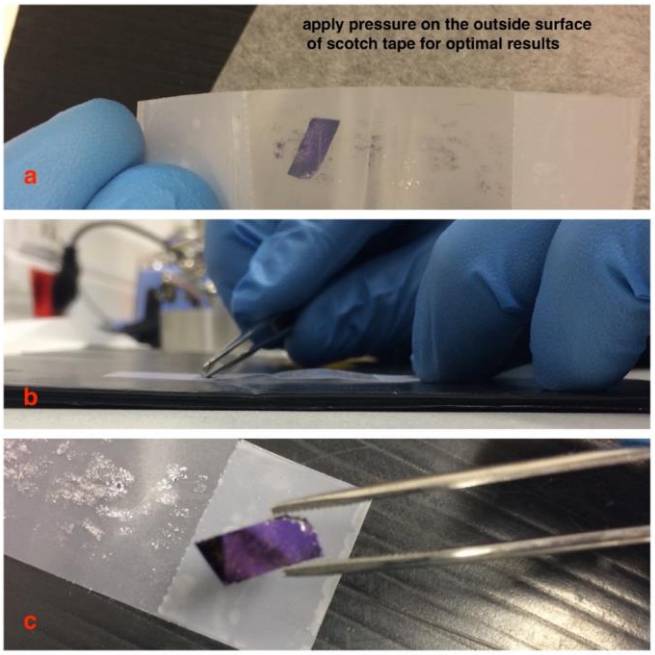

Figure 3.6: a) Pressure application on the external side of scotch-tape. b) Pealing the substrate off the scotch-tape. c) Free-standing substrate containing exfoliated GeSe flakes.

Now that the substrate contains several exfoliated flakes, we set it under an optical microscope and look for possible areas that they may contain few layers of GeSe.

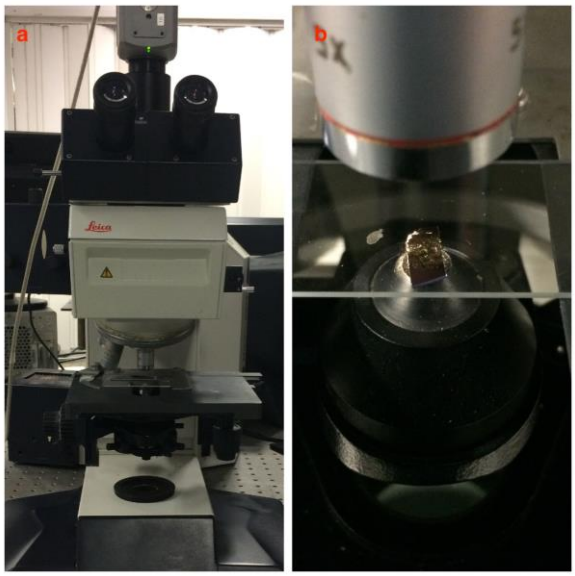

Figure 3.7: a) Leica optical microscope we used to investigate our samples. b) Substrate placement under the microscope.

3.2.2 Thermal annealing combined with scotch-tape exfoliation

The second exfoliation procedure we tried was a combination of the mechanical exfoliation described previously and thermal annealing. After scotch tape exfoliation, we place the substrate that contains GeSe flakes in a ceramic boat-shaped device and in an oxidation oven which we sealed. We performed several trials for this experiment to find the optimal settings that could provide us with few-layer GeSe flakes **[43, 44]**.

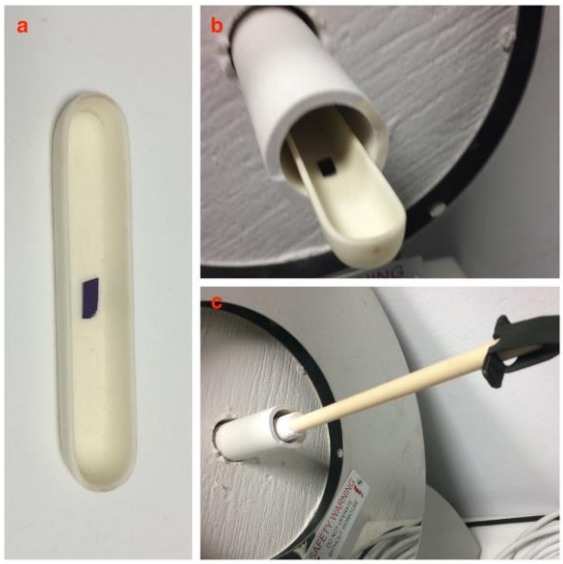

Figure 3.8: a) Substrate placed in a ceramic boat after scotch-tape exfoliation. b) Boat inserted in the oxidation oven via a tube. c) Oxidation oven was sealed with the plugs shown

3.2.3 Laser thinning

The last experimental procedure we used was a combination of scotch-tape exfoliation and laser thinning **[45, 46]**. Again, we prepared and transferred exfoliated flakes of GeSe on a SiO_2 substrate with standard mechanical exfoliation. Then, using the laser of the Raman setup, we performed a series of experiments with different exposures and laser power adjustments to thin down the flakes while acquiring Raman spectra for each set of settings at the same time. This was a straight forward experiment and we were able to perform experiments using both wavelengths available on the Raman setup (473nm and 780nm).

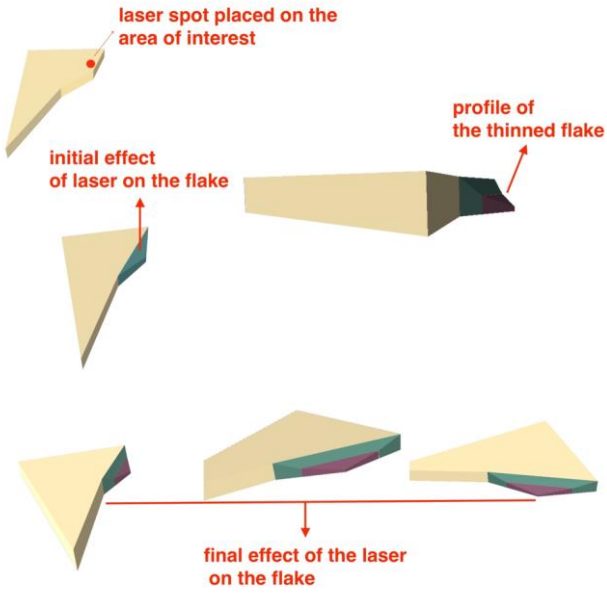

Figure 3.9: Morphological evolution and profile of the laser-thinned flake. The color differentiation corresponds to different thicknesses

The setup we used for material characterization and laser thinning was the Nicolet Almega XR Micro Raman analysis system which is equipped with a diode-pumped solid-state laser (DPSS) offering the ability to work both with 473nm and 780 nm laser lines (see section 3.1). The system consists of a confocal single monochromator spectrometer and we can move around and focus on our samples using the scanning motorized stage and the 100x Olympus objective lens (with numerical aperture of 0.9) that are included in the setup. The maximum output power is 50mW and it is controlled with a neutral density filters. The signal is analyzed by a high-resolution grating (2400 lines per mm).

II. Experimental Results and Analysis

4. Mechanical Exfoliation

The first exfoliation procedure we followed to reach few-layers of GeSe, was the well-known "scotch-tape" technique. Even though this exfoliation method is proven to work very well for TMDs, it doesn't do so in the case of GeSe crystal. After series of experimentation, our data revealed the same profile repeatedly. The exfoliated flakes that we managed to produce were nowhere near the single or bi-layer limit. Their appearance under the microscope (compared with other exfoliated crystals) was closer to few hundreds of layers than just few-layer structure. In addition, we observed no change or shift in their Raman spectra in comparison with the already known bulk spectra. Since using this exfoliation method we couldn't produce a sample thin enough, it may be that the forces between the layers is not just van der Waals and this could explain why there is still no report of monolayer GeSe. In Figs.4.1 and 4.2, the Raman spectra of two samples prepared with scotch-tape exfoliation are shown. We used the 780nm excitation wavelength and kept the power very low to a level of 1% of the maximum power (which corresponds to 7kW/cm^2) in order to avoid any damage from the laser. The exposure time used was increased to 20 seconds (accounting the fact that we used 1% of the laser power) in order to reduce the noise in the spectra. The main Raman modes we observed were at 150 cm^{-1}, 175 cm^{-1} and 190 cm^{-1} and agree very well with the already reported modes for the bulk GeSe crystal and correspond to B_{3g}, A^2_g, and A^1_g vibrational modes respectively. There were changes in the intensity of the modes between different flakes which we have assigned them to different sample-thickness. From the comparison of Fig.4.1 with Fig.4.2, there is an almost three-fold drop in the

intensity of the vibrational modes of GeSe implying that sample 1 is thicker than sample 2. This conclusion is supported by the fact that the intensity of the Si peak from the substrate (at 520 cm-1) is more than 3 times lower in sample 1 than sample 2 (the Si-peak intensity increases from 800 to 3250 counts)

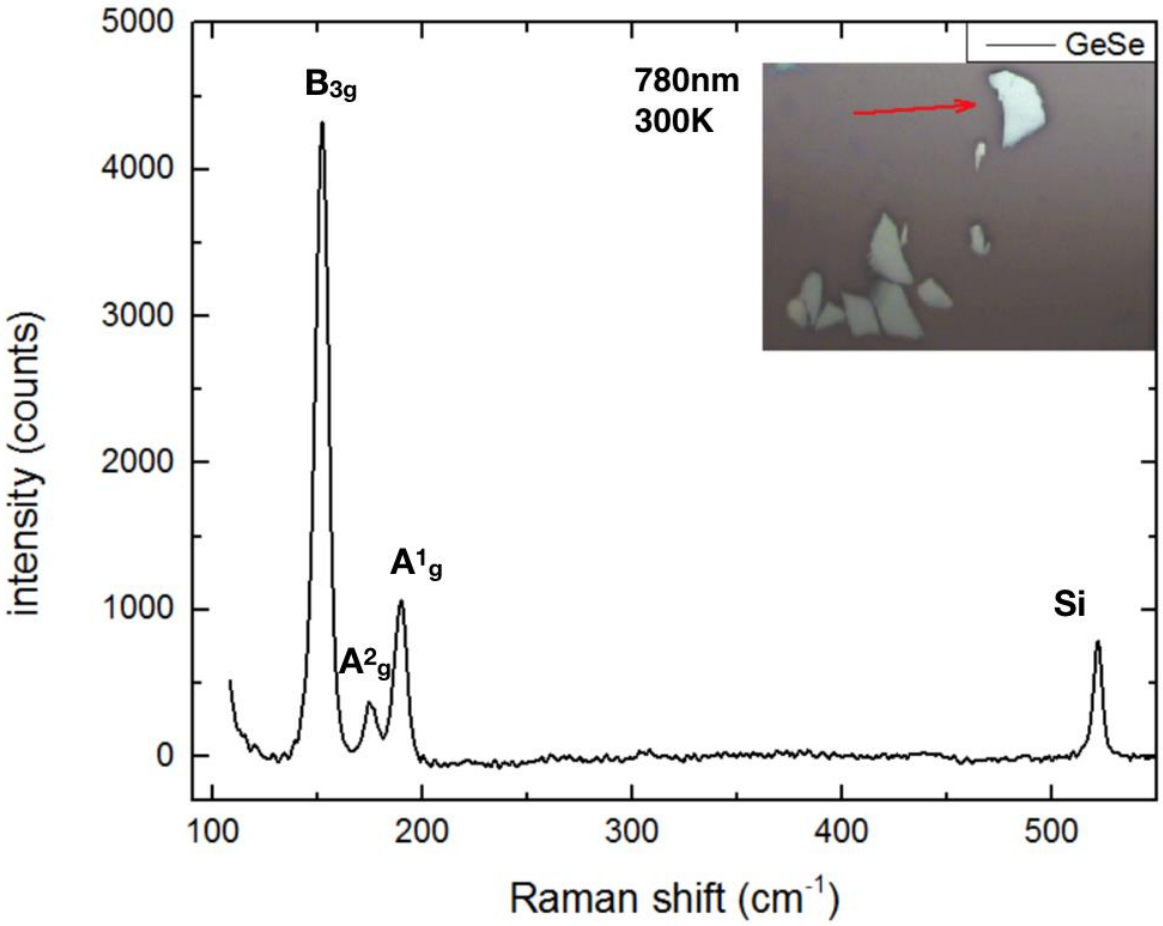

Figure 4.1: Raman spectrum of exfoliated sample 1 taken with 780nm excitation. The Raman modes at 150cm^{-1}(B_{3g}), 175cm^{-1} (A^2_g) and 190cm^{-1}(A^1g) completely agree with the bulk GeSe reference spectra. The red arrow indicates the flake we used to obtain the spectrum.

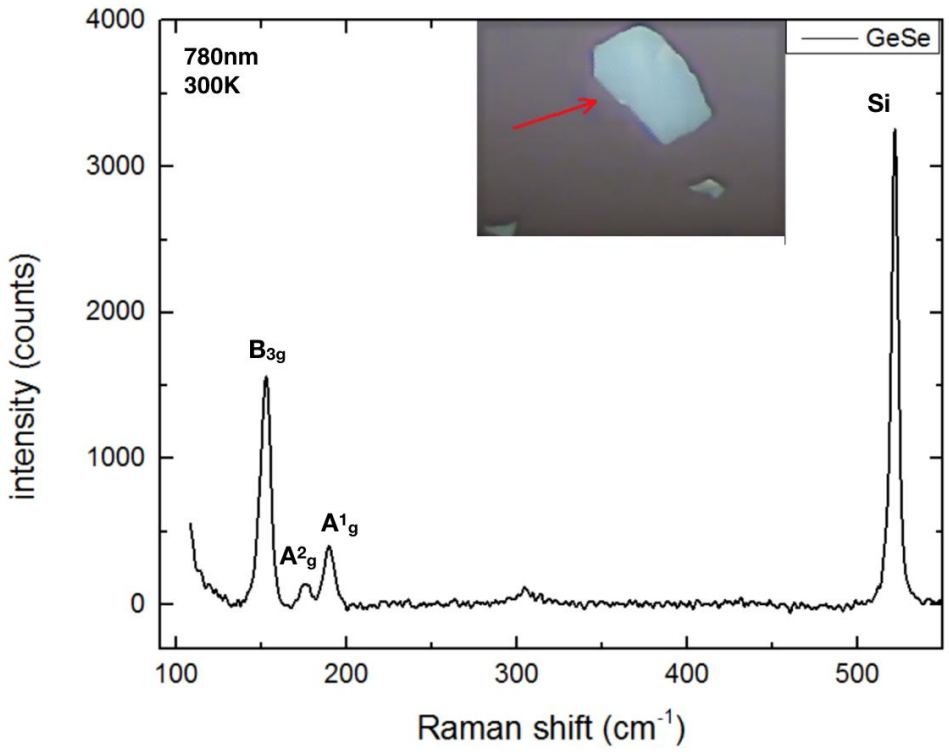

Figure 4.2: Raman spectrum of exfoliated sample 2 taken with 780nm excitation. No energy shift of the main Raman modes is observed. On the other hand, there is a significant intensity reduction of the GeSe modes with a simultaneous increase in the intensity of the Si-peak. This means that sample 2 is thinner than sample 1.

5. Thermal annealing

Considering that with conventional scotch-tape exfoliation we couldn't manage to reach our target which was few-layer GeSe structure, we focused on exploring other exfoliation techniques to validate our previous results and find a single or double-layer GeSe flakes. To this end, we performed annealing combined with scotch-tape exfoliation. First, using scotch tape, we exfoliated a new sample and then we performed thermal annealing in air. We used this technique because there are reports of experiments on MoS_2 with very promising results reaching down to even a single-layer. We performed a series of experiments trying to find the best settings (time and temperature) in order to create thin flakes of GeSe. Even though there was no stability for our results, optimal data were obtained with **thermal annealing for 5 hours at 375ºC**. The results were promising since GeSe

flakes seemed, under the microscope, to show a variation in thickness. Moreover, changes in their appearance were obvious comparing them to flakes coming out after simple scotch-tape exfoliation. The next step was characterization of these flakes with Raman spectral analysis and AFM measurements in order to validate whether thermal annealing did help in creating thinner GeSe structures. Upon collecting the first Raman spectra of our annealed samples, we observed that the signal was not so strong. This led us to change the laser line from 780 nm to a shorter wavelength (473nm) taking advantage of the higher energy. There was a big difference in the Raman spectra compared to the well-known vibrational modes of bulk GeSe. The three main characteristic modes we have discussed previously were absent for the most part and two new modes appeared. These new modes were at energies of 119 cm^{-1} and 212-213 cm^{-1}. This led us to believe that we did performed a change in GeSe crystal's phase but still we had to identify the nature of this change. Typically for other crystals, when we reach the monolayer or bilayer limit, there is a shift in Raman spectra. In our case we had to deal with new modes and the disappearing of the initial dominant Raman modes.

In the following figures we show optical images, AFM measurements for thickness characterization and the corresponding Raman spectra for several flakes. The thinnest GeSe flake

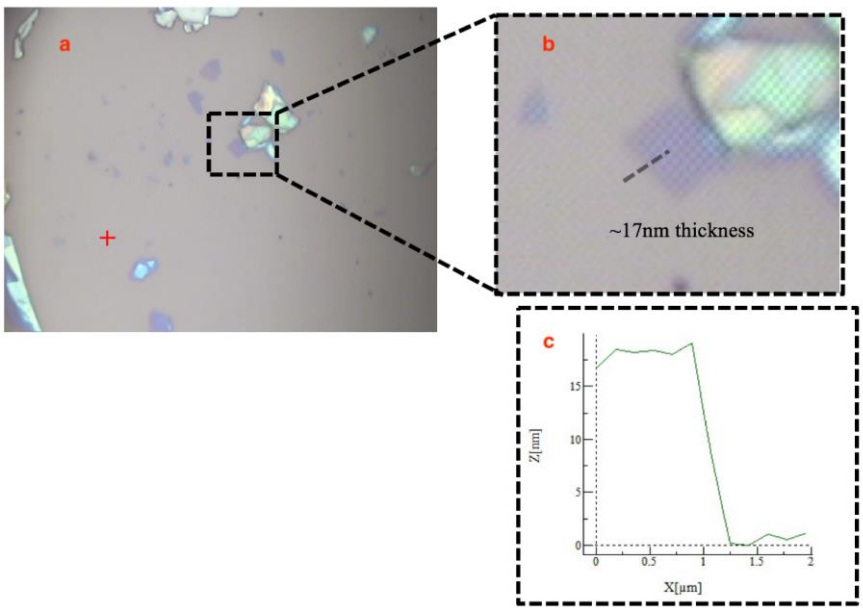

Figure 5.1: AFM measurements of the flake of interest. a) the purple square-like flake inside the black dashed square is the one measured. b) The black dashed line shows the movement of the tip. c) AFM thickness measurement (17nm).

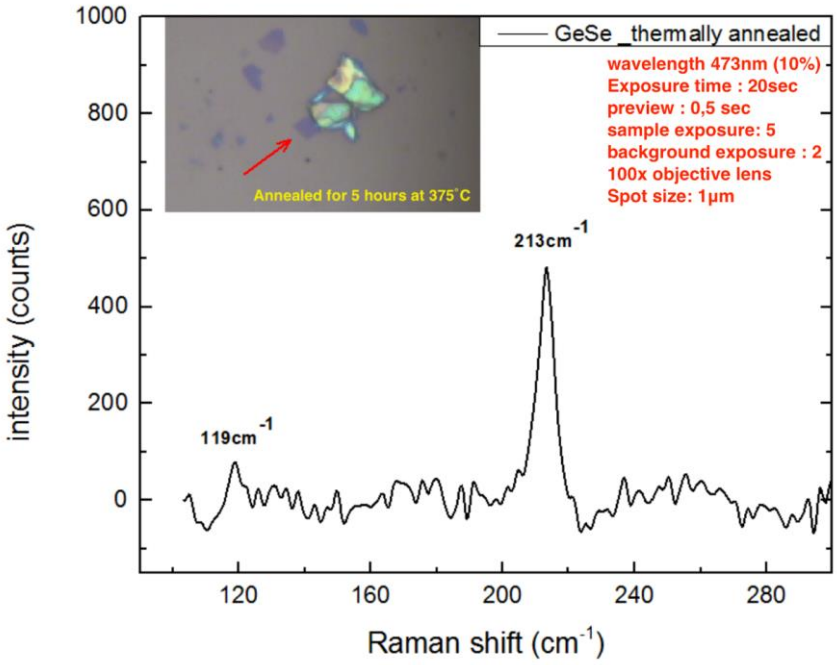

Figure 5.2: Raman spectra of annealed GeSe flake. The red arrow indicates the area from which we took the spectrum.

(Fig.5.1) we achieved was characterized with atomic force microscopy and it was found to be 17 nm thick. This size corresponds to approximately a 20-layer of GeSe structure. The Raman spectrum for this flake is shown in **Fig.5.2** where the mode at 213 cm^{-1} is the dominant one. Two more thicker flakes whose thickness was measured by AFM to be 45 nm and 160 nm **(Fig.5.3 and 5.5)**, were studied and their corresponding Raman spectra are shown in **Figs.5.4 and 5.6** respectively. We also observe that the dominant modes at 150 cm^{-1}, 175 cm^{-1} and 190 cm^{-1} for the GeSe are toned down to level that we cannot see them anymore in most of the cases.

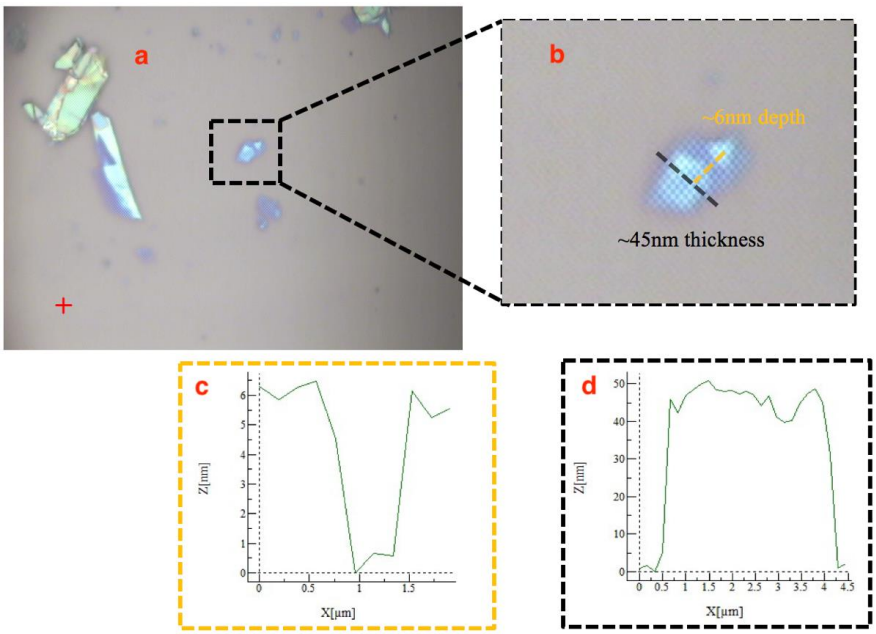

Figure 5.3: a) Optical image. The area of interest is shown inside the dashed square. b) Black dashed line shows the movement of the tip measuring the thickness and orange dashed line shows the movement of the tip c) AFM graph of the gap and d) AFM thickness measurement (45nm)

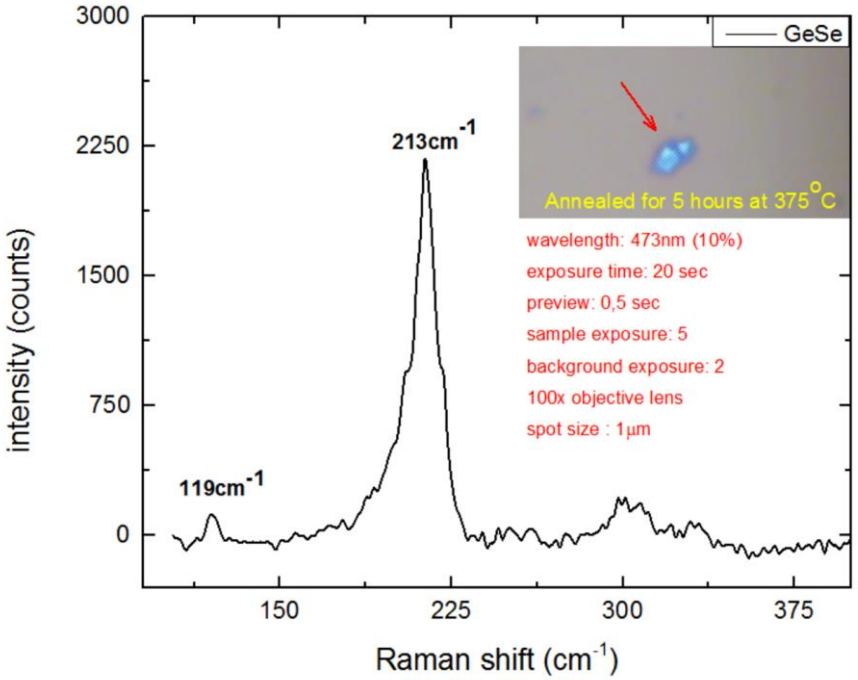

Figure 5.4: Raman spectrum of thermally annealed area shown by the red arrow (this flake presented a small gap after the experiment)

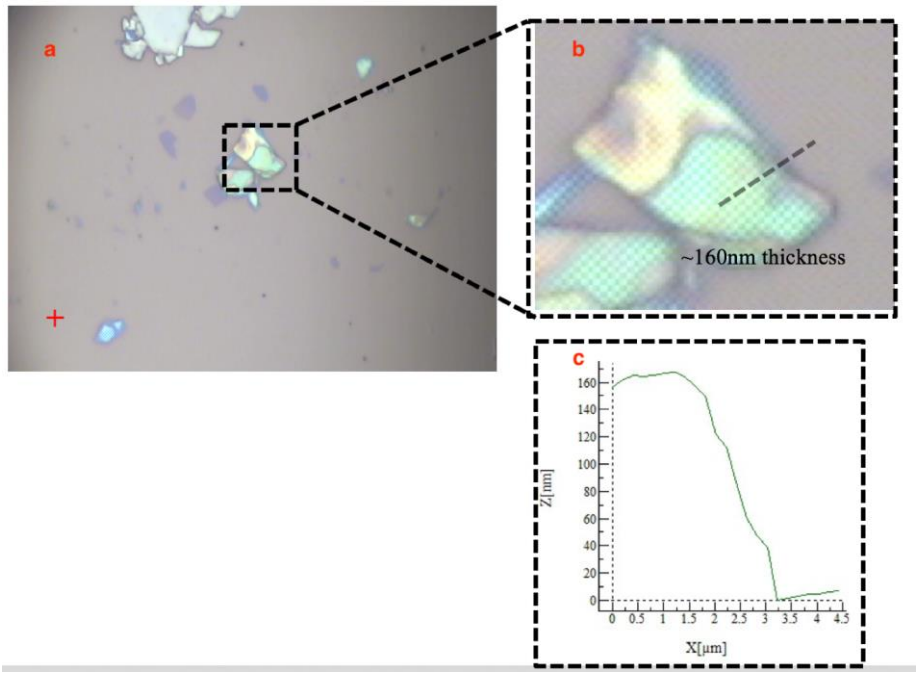

Figure 5.5: a) The green area of the flake inside the dashed square is the one we took AFM measurements. b) The black dashed line shows the movement of the tip. c) AFM graph showing the thickness of the flake (160 nm)

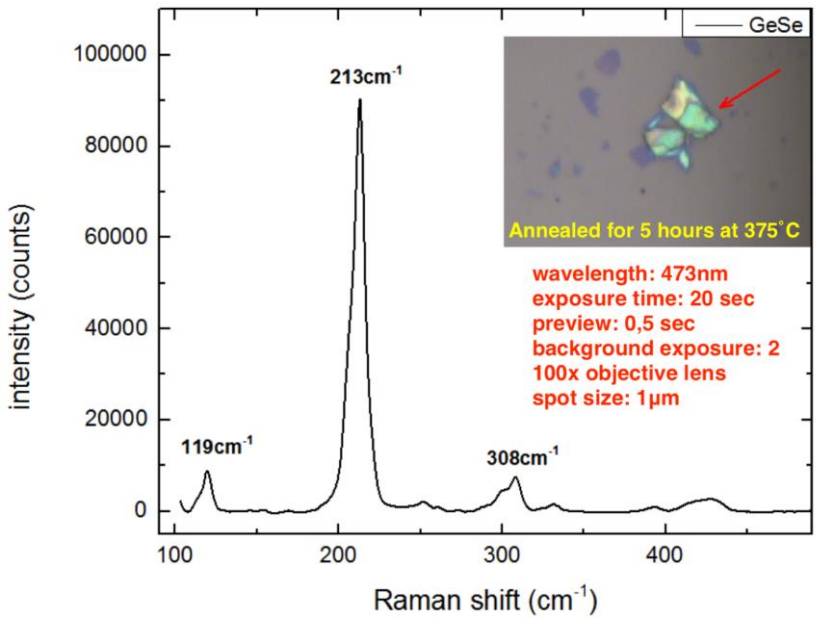

Figure 5.6: Raman spectrum of thermally annealed area shown by the red arrow

For the last flake (160nm thick), we observed another mode at 308cm^{-1} but still the dominant modes are at 119cm^{-1} and 213cm^{-1}. This difference in thickness between the 17nm flake and the 160nm flake is expected due to their morphological appearance since for crystals exfoliated to few-layer structures the appearance matches the one of 17nm flake.

We have also studied a flake, that was thermally annealed under the same exact settings as the ones in Fig. 5.1, 5.3 and 5.5 but revealed different Raman spectra.

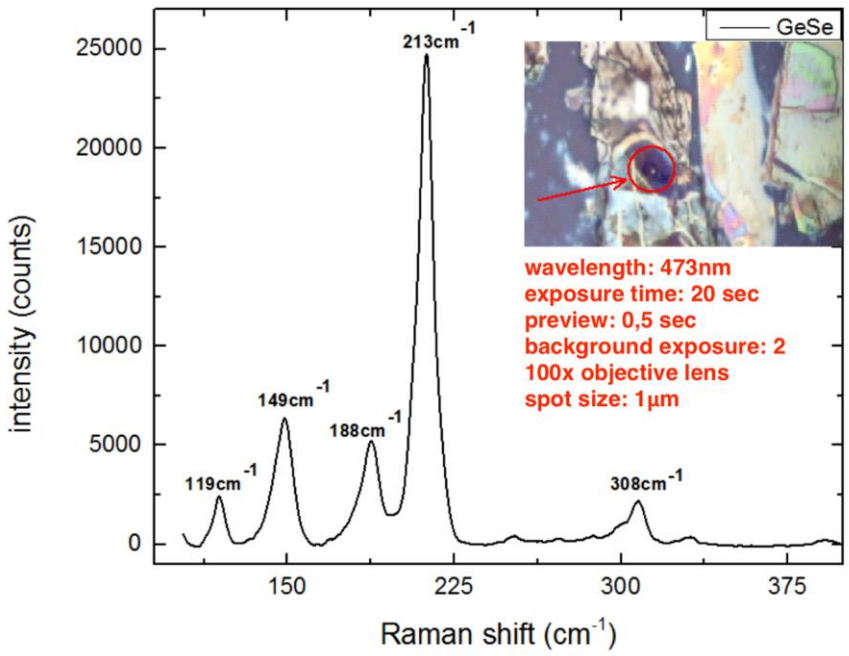

Figure 5.7: The purple area inside the red circle is the one of interest that corresponds to the embedded Raman spectrum.

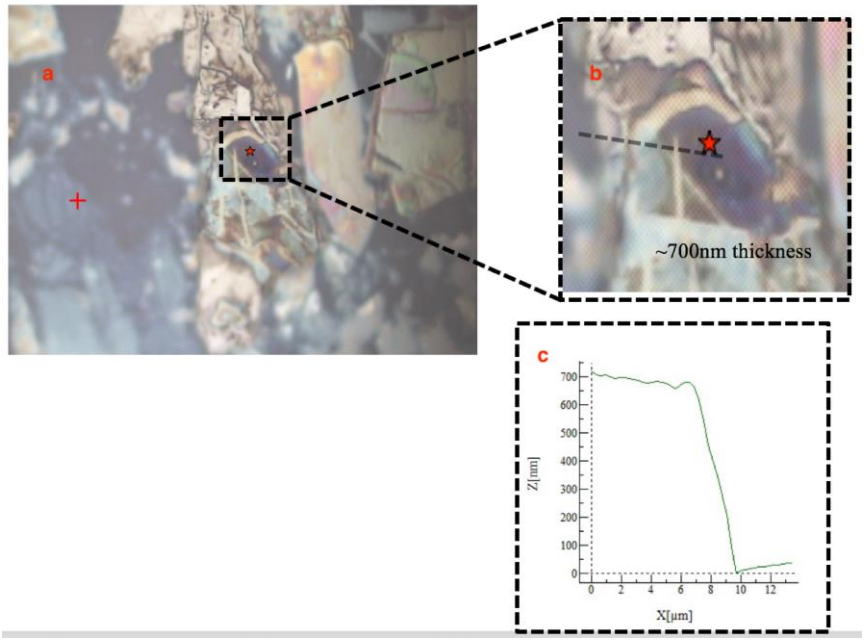

Figure 5.8: a) Optical image of the flake. b) The dashed line is showing the movement of the tip and the red star is placed at the exact spot where the laser hit the target. c) AFM graph showing the thickness of our target for the specified area (700nm).

Even though this last target of GeSe crystal resembles few-layer structures after annealing, it proved to be the thickest of our GeSe samples (almost 700 nm) as shown in AFM analysis in Fig. 5.8. The Raman spectrum **(Fig.5.7)** was really interesting for this target since it revealed not only the new modes (119 cm^{-1}, 213 cm^{-1}, 308 cm^{-1}) that we systematically observed for the other thinner areas too, but also the modes of bulk GeSe crystal that we've seen for targets after only scotch-tape exfoliation. The only difference was that for the later target there is a red shift with vibrational modes placed at 149 cm^{-1} and 188 cm^{-1} respectively.

It well known that GeSe is an anisotropic material and that's the reason we decided to perform an angle Raman study on the thinner and the thickest samples.

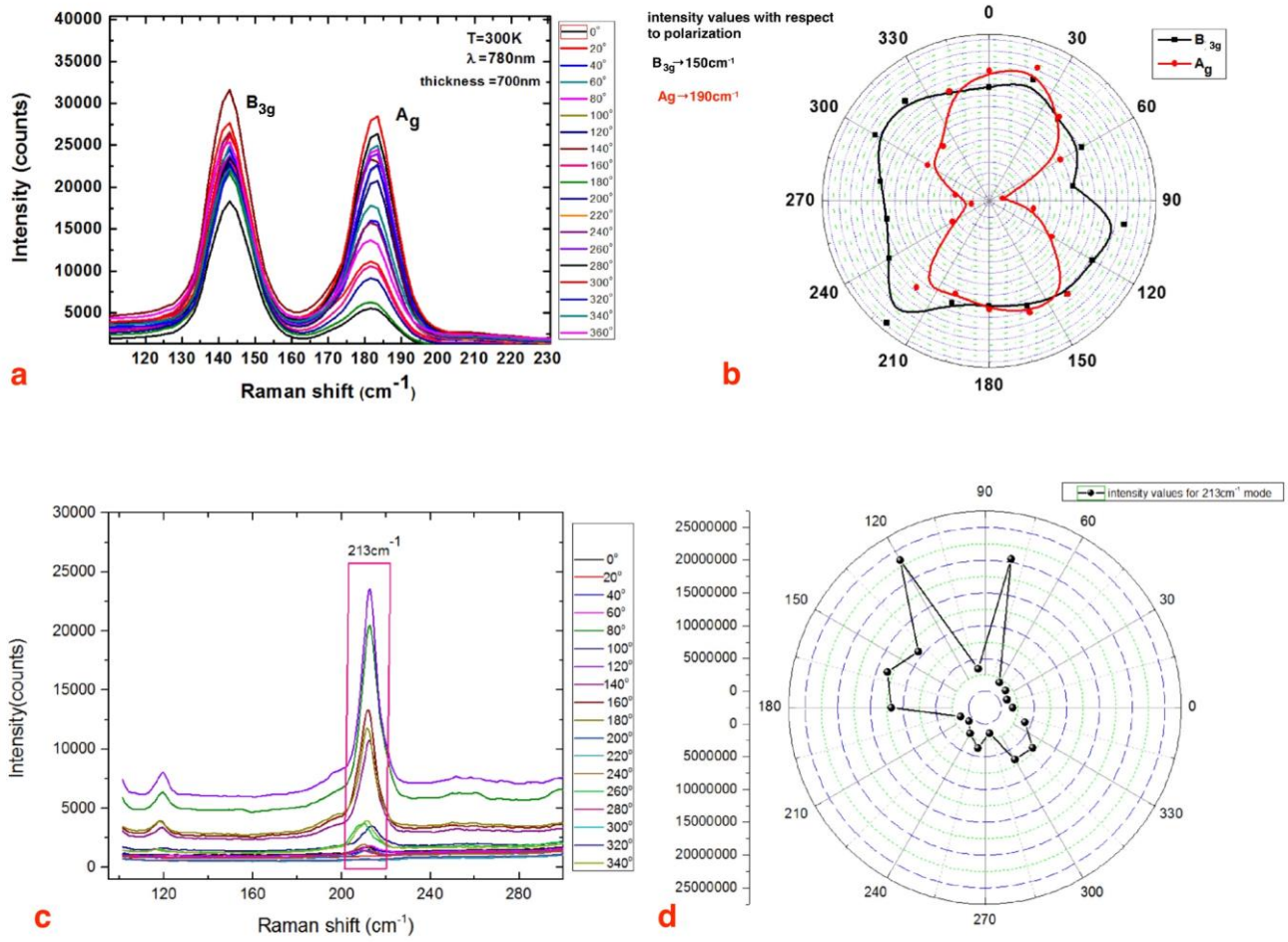

Figure 5.9: (a-b) Angle-related Raman study of 700nm sample. (c-d) Angle-related Raman study of 17nm sample.

The results in the **figure 5.9** revealed differentiation between the periodic behavior of dominant vibrational modes we observed. For the 700nm sample we can see that both dominant modes are present regardless the orientation of the sample. Moreover, there is periodicity in their intensity values with respect to polarization (more for A_g, less for B_{3g}). In contrast, the 17nm sample doesn't reveal any periodic behavior whatsoever. In addition, for certain angles the signal approaches zero.

6. Thermal annealing combined with laser thinning

Since thermal annealing gave us thinner flakes of GeSe in contrast with simple scotch-tape exfoliation, we thought that this method might help us reach the ultimate target which was single or double-layer flakes despite the remarkable differences in the Raman spectra compared to bulk GeSe.

While taking Raman measurements on the thicker annealed samples (like the 700nm sample that we have shown earlier), we observed that the intensity of the main GeSe dominant peaks was decreasing during a single data collection time. In addition, we could clearly see morphological changes on the surface of the flakes. In Fig.6.1, we show optical images taken during collective Raman measurements on a typical sample of intermediate thickness. The images were taken right after the Raman measurement with the 780nm laser line (70KW/cm2). We clearly see changes in the contrast on the surface. This motivated us to try the combination of thermal annealing and laser thinning aiming to push further the limits of the GeSe thickness. We created samples with thermal annealing and then we used the Raman setup's laser line to thin further down the flakes.

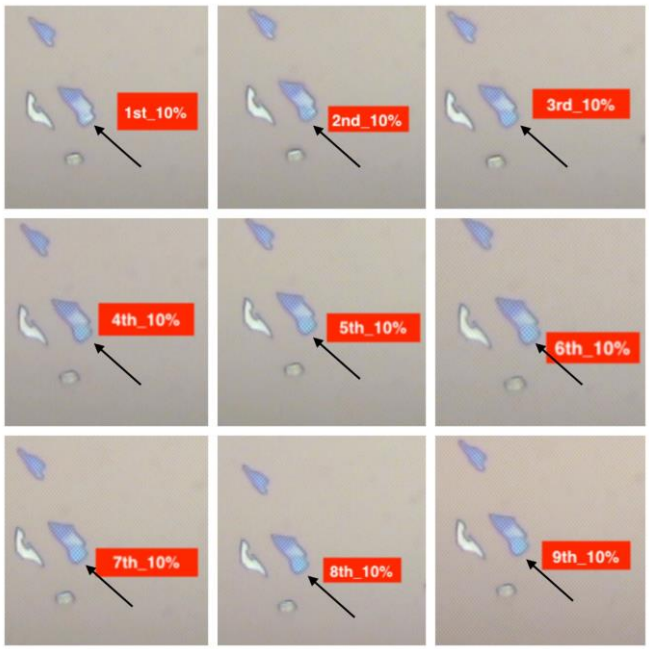

Figure 6.1: Morphological changes of the annealed area while we hit repeatedly with 780nm wavelength (10%)

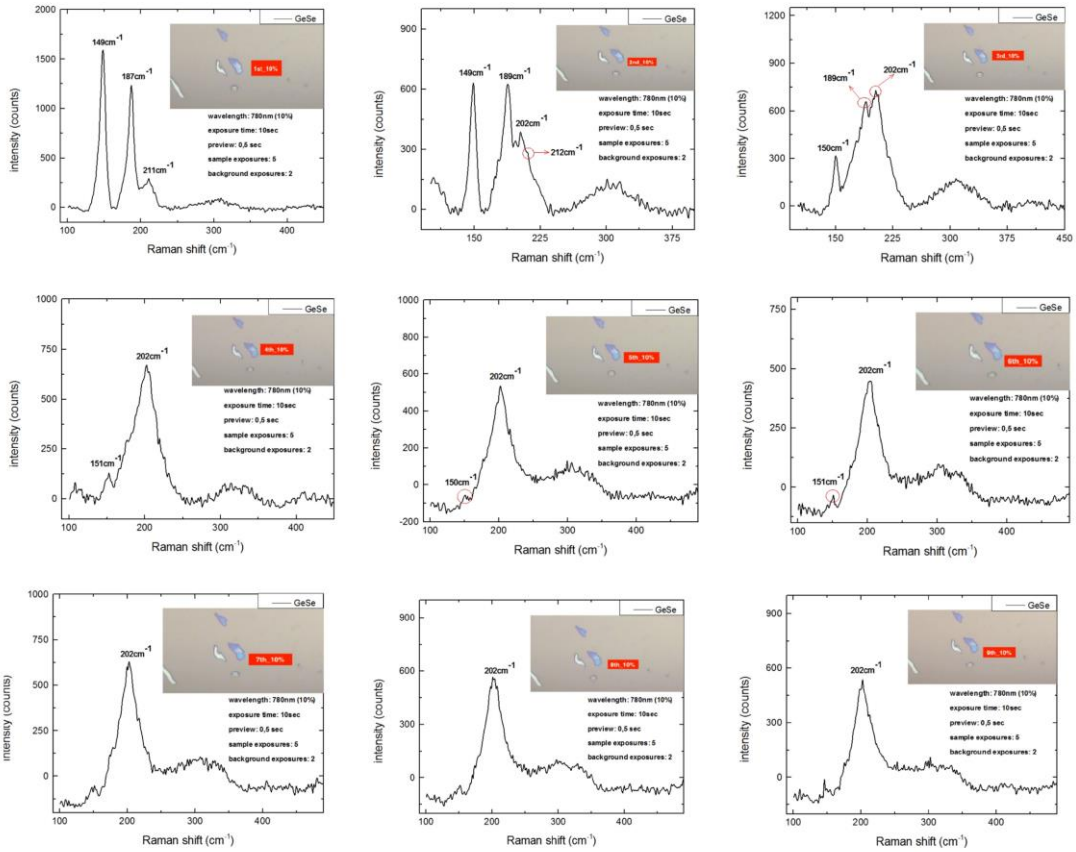

Figure 6.2: Raman spectra of the annealed area thinned down with the laser

In Fig.6.2, we plot the Raman spectra that correspond to the images shown in Fig.6.1. At first, we can see that in the very first spectra, we have both the dominant modes of bulk GeSe placed at 149cm^{-1} and 187cm^{-1} while at the same time we can also observe the mode placed at 211cm^{-1} which is related to thermal annealing experiment we performed before. The small shifts we observe in this case are mostly due to the different GeSe crystal we used for this experiment.

At the early stages of this experiment, we can clearly see that bulk modes are tuned down (the 149cm^{-1} survives but the intensity is decreased) fast and that we also lose the mode at 211cm^{-1}. On the other hand, a mode at 202cm^{-1} rises fast, becomes the dominant mode in our spectra and stabilizes as far as intensity is concerned.

The last part of this experiment was to increase the intensity of the 780nm laser line to 16%, 25%, 50% and 100% (1200 KW/cm2) aiming to test the limits of thermal annealing and laser thinning combination (Fig.6.3). The corresponding Raman spectra are depicted in Fig.6.4 where we see that

we had lost all the initial modes. In addition, the new mode placed at 202cm^{-1} survived the whole procedure.

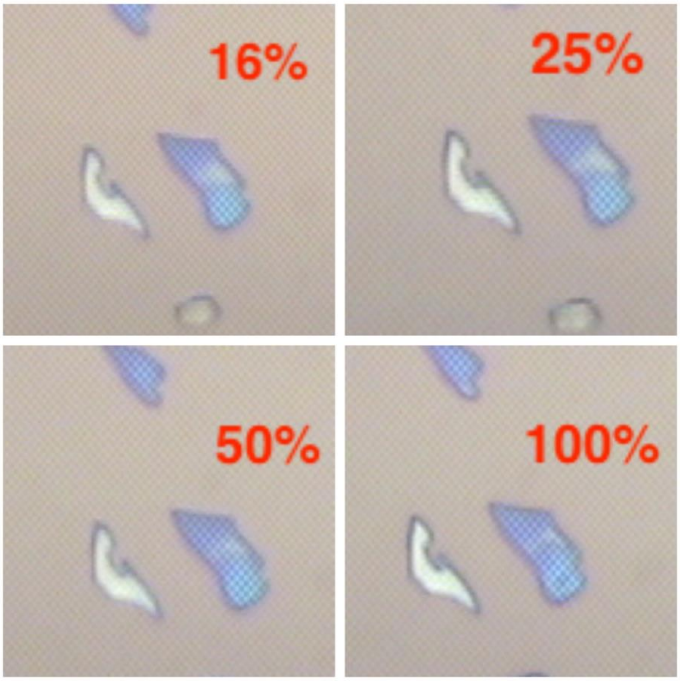

Figure 6.3: Morphological changes due the power of the 780nm laser line

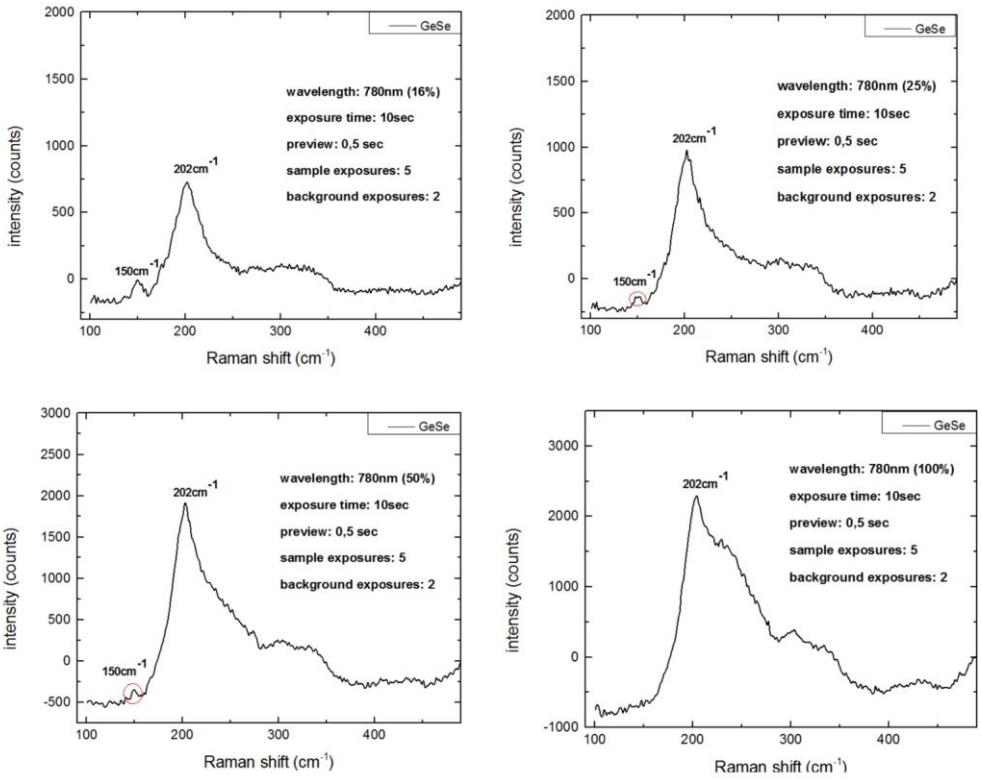

Figure 6.4: Raman spectra related to the flake of interest with respect to intensity variation

7. Laser thinning of bulk pristine GeSe flakes

Considering the differentiations of Raman modes with respect to exfoliation techniques, we decided to perform laser thinning on GeSe flakes created by "scotch-tape" exfoliation with no thermal treatment. This way we aimed to get a more complete picture about what is changing on a GeSe flake regarding each exfoliation technique applied. To this end, we created GeSe flakes with "scotch-tape" exfoliation and we placed them into the Raman setup for laser thinning. We used both the available wavelengths 780nm and 473nm.

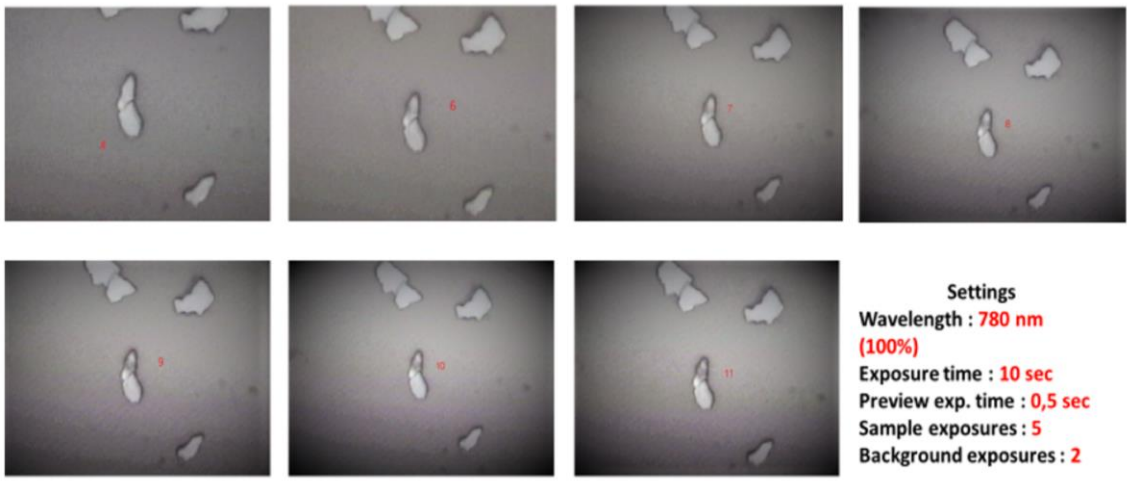

Figure 7.1: Evolution of the flake's morphology over multiple data acquisition

For our first approach, we tried laser thinning with 780nm wavelength hitting the flake multiple times

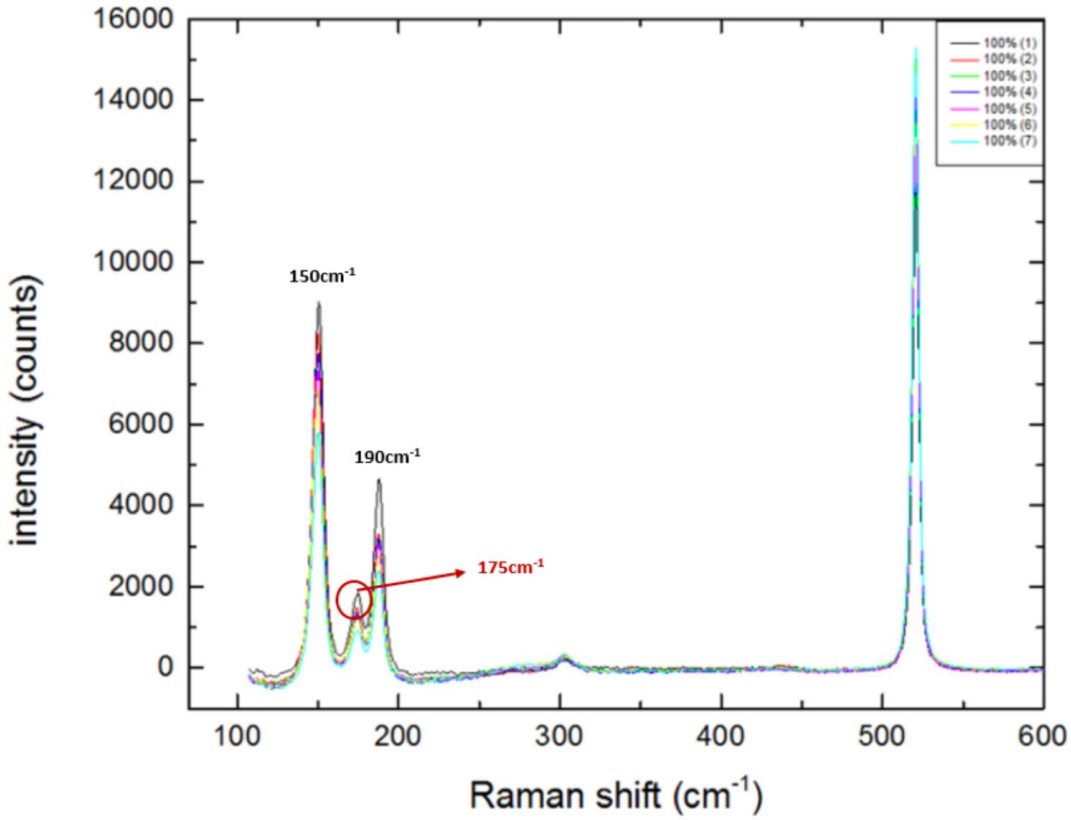

Figure 7.2: Raman spectra during data acquisition for the laser thinning experiment with 780nm wavelength.

with 100% power as shown in figure 7.1. The corresponding Raman spectra shown in Fig.7.2, revealed no change in main pristine GeSe vibrational modes. The main modes of bulk GeSe crystal survived the whole experiment with this particular set of settings.

The next step on laser thinning experiment was to use the other available wavelength, 473nm, to fully evaluate the resulting data. To this end, initially we performed the experiment by gradually changing the intensity of the laser hitting the surface of our flake (Fig.7.3). We did so, because 473nm is a shorter wavelength and therefore the energy that reaches our flake is bigger than before.

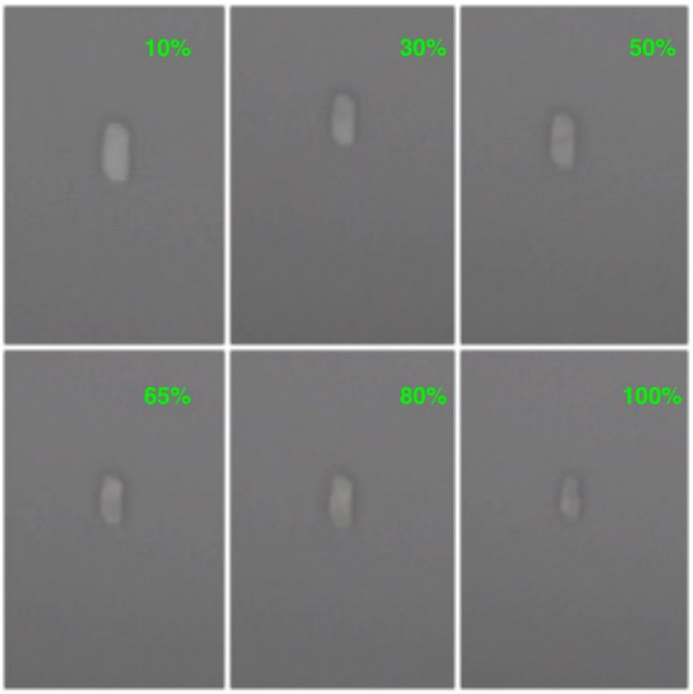

Figure 7.3: Evolution of the flake's morphology during laser thinning with 473nm as function of the laser power

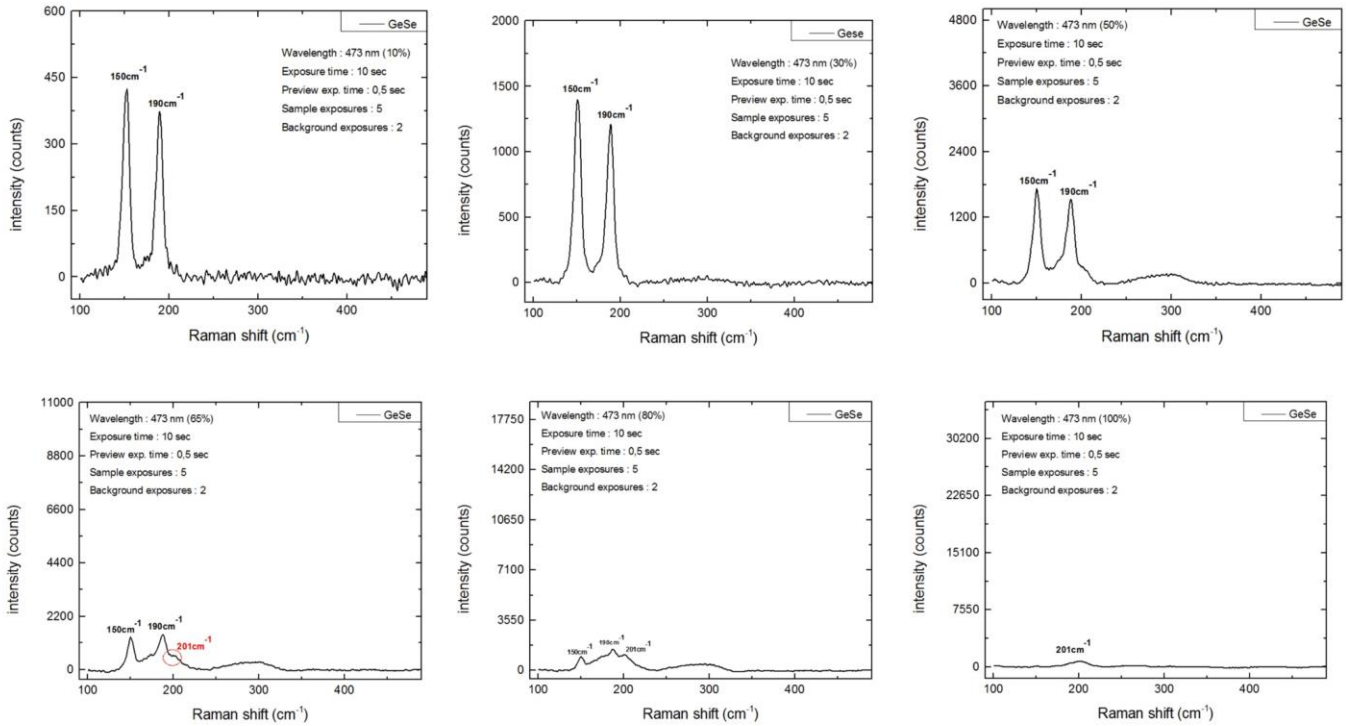

Figure 7.4: Raman spectra during data acquisition for the laser thinning experiment with 473nm wavelength with respect to intensity values.

Fig.7.4 shows the corresponding Raman spectra. We observed a mode at 201cm^{-1} rising at the spectrum corresponding to 65% intensity of the laser while in the meantime there was a constant decreasing of the bulk modes during the experiment. At the end, reaching 100% of intensity the only mode that survived was at 201cm^{-1}. This mode was not as sharp, and it was maintained at low intensities. Moreover, we didn't observe any mode between 211cm^{-1} and 213cm^{-1} in contrast to experiments with thermal annealing involved.

The last step for this series of experiments was repeating laser thinning with the 473nm laser line while keeping the intensity at 100% for all measurements (Fig.7.5).

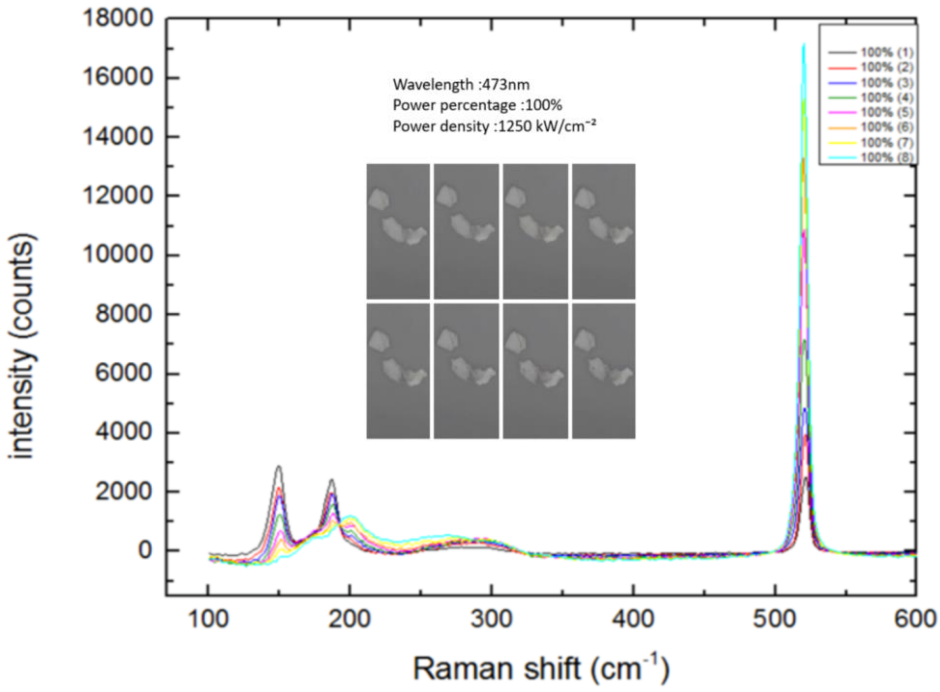

Figure 7.5: Evolution of the GeSe flake's morphology and Raman modes during laser thinning with 473nm at 100% power (1200 kW/cm^{-2}).

The results were very much like the previous experiment where we could see the changes in the Raman spectra but this time our flake was rather thicker than before. Therefore, to evaluate the thinning, we had to monitor the intensity of the Si Raman mode at 521 cm^{-1} (Fig.7.6). As we see in this figure, the intensity of the Si peak increases upon thinning the flake.

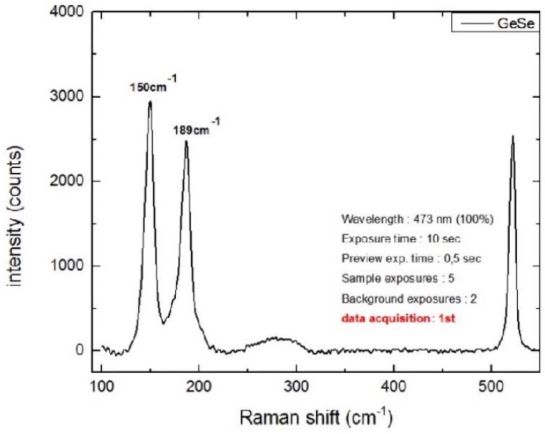
GeSe
150cm-1
189cm-1
Wavelength : 473 nm (100%)
Exposure time : 10 sec
Preview exp. time : 0,5 sec
Sample exposures : 5
Background exposures : 2
data acquisition: 1st
intensity (counts)
Raman shift (cm-1)

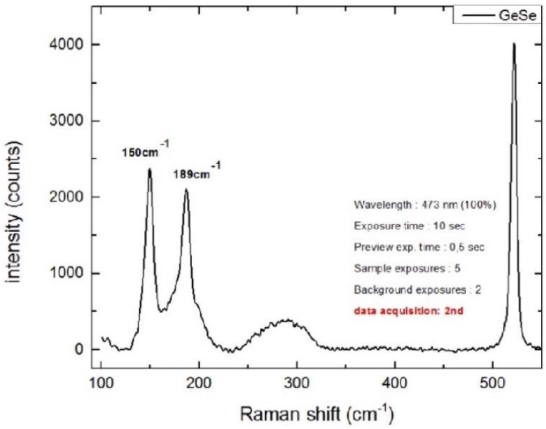
GeSe
150cm-1
189cm-1
Wavelength : 473 nm (100%)
Exposure time : 10 sec
Preview exp. time : 0,5 sec
Sample exposures : 5
Background exposures : 2
data acquisition: 2nd
intensity (counts)
Raman shift (cm-1)

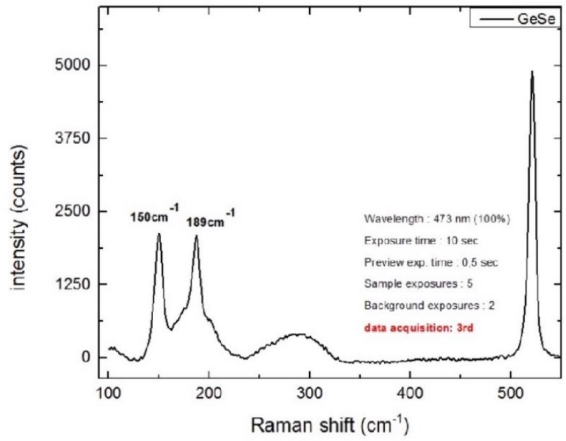
GeSe
150cm-1
189cm-1
Wavelength : 473 nm (100%)
Exposure time : 10 sec
Preview exp. time : 0,5 sec
Sample exposures : 5
Background exposures : 2
data acquisition: 3rd
intensity (counts)
Raman shift (cm-1)

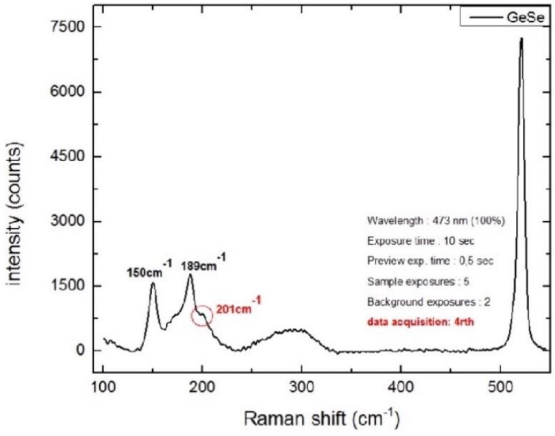
GeSe
150cm-1
189cm-1
201cm-1
Wavelength : 473 nm (100%)
Exposure time : 10 sec
Preview exp. time : 0,5 sec
Sample exposures : 5
Background exposures : 2
data acquisition: 4rth
intensity (counts)
Raman shift (cm-1)

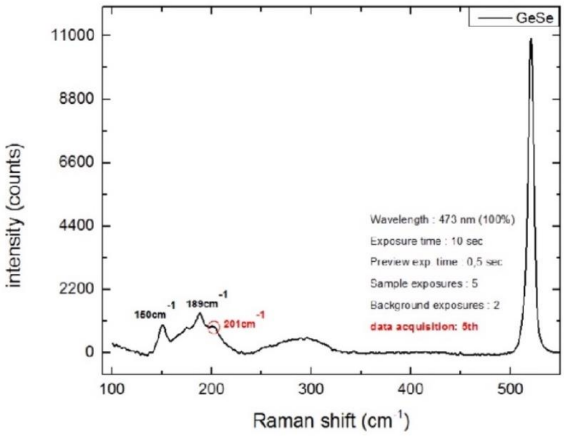
GeSe
150cm-1
189cm-1
201cm-1
Wavelength : 473 nm (100%)
Exposure time : 10 sec
Preview exp. time : 0,5 sec
Sample exposures : 5
Background exposures : 2
data acquisition: 5th
intensity (counts)
Raman shift (cm-1)

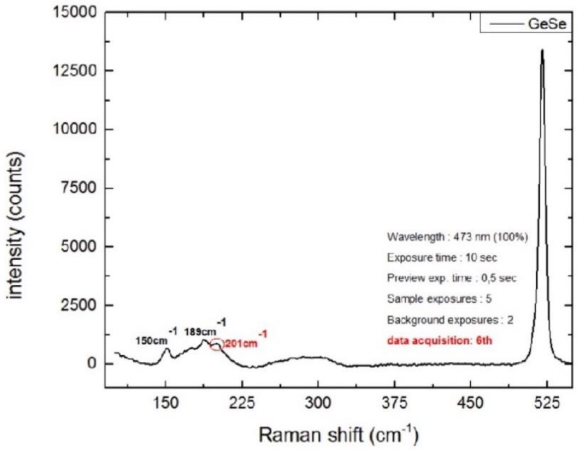
GeSe
150cm-1
189cm-1
201cm-1
Wavelength : 473 nm (100%)
Exposure time : 10 sec
Preview exp. time : 0,5 sec
Sample exposures : 5
Background exposures : 2
data acquisition: 6th
intensity (counts)
Raman shift (cm-1)

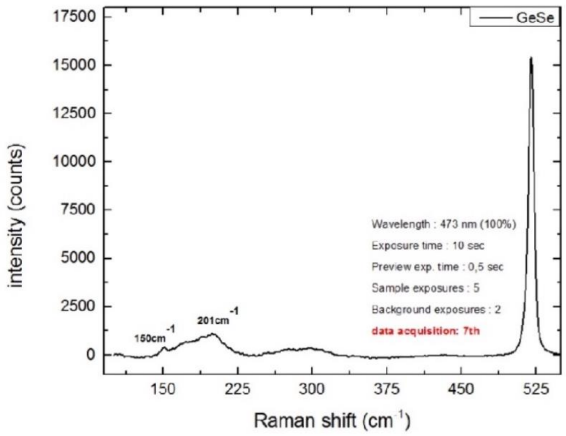
GeSe
150cm-1
201cm-1
Wavelength : 473 nm (100%)
Exposure time : 10 sec
Preview exp. time : 0,5 sec
Sample exposures : 5
Background exposures : 2
data acquisition: 7th
intensity (counts)
Raman shift (cm-1)

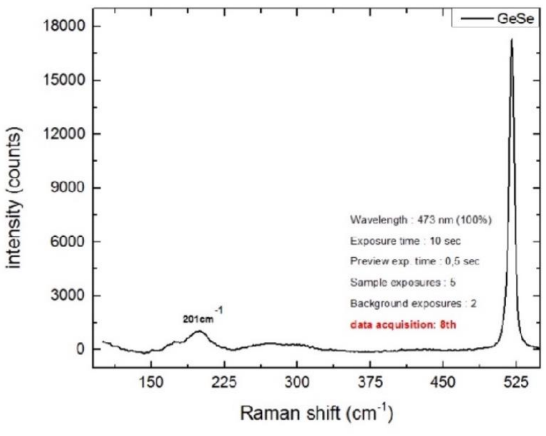
GeSe
201cm-1
Wavelength : 473 nm (100%)
Exposure time : 10 sec
Preview exp. time : 0,5 sec
Sample exposures : 5
Background exposures : 2
data acquisition: 8th
intensity (counts)
Raman shift (cm-1)

Figure 7.6: Collective Raman spectra showing the evolution of Raman modes for GeSe flake during multiple acquisitions.

In Fig. 7.7a we plot the intensity of the main Raman modes taken from Fig. 7.6 as a function of the time the flake is exposed to the laser. A clear intensity decrease of the pristine GeSe vibrational modes is observed. After a total exposure of 40 seconds, the 201cm^{-1} mode appears and dominates the spectrum. On the other hand, the Si peak's intensity is constantly increasing during laser thinning of the material as shown in Fig. 7.7 b which clearly indicates the thinning of the sample.

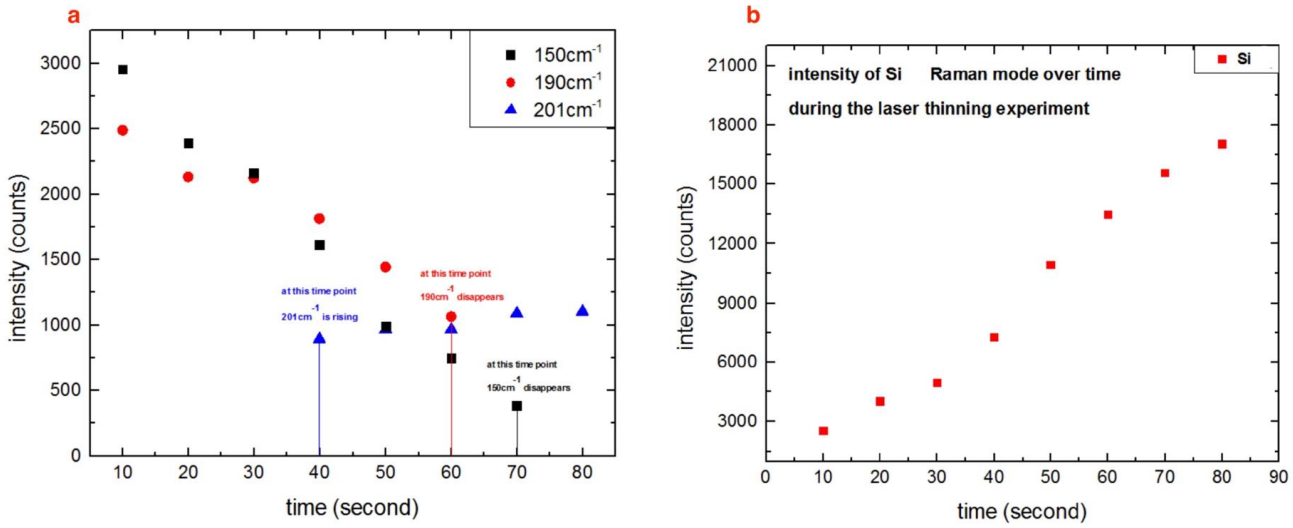

Figure 7.7: a) Intensity over time plot of Raman modes for laser thinning with 473nm at 100% power. b) intensity over time plot of Si Raman mode at 521cm^{-1}.

8. Discussion

The goal of this thesis was the isolation of single or double-layer GeSe and the evaluation of well-established techniques that can lead us to few-layer structures. To this end, we initially performed the well-known mechanical exfoliation (scotch-tape) technique that works very well for

the TMDs. However, we this method we could only get thick multilayer GeSe samples. The failure to produce monolayers or bilayers, most likely, is linked to the type of bonding between the crystal's layers. Even though theory predicts van der Waals bonding, our flakes were typically dozens of nanometers thick implying a covalent-like bonding between the layers.

Our first approach was to find a way to induce an amount of energy to weaken the bonding between the layers and get thinner flakes close to a monolayer. The thermal annealing, as a thinning method, worked very well for the TMDs producing thin flakes without compromising the structural properties of the sample. Motivated by these reports we combined the scotch tape exfoliation technique with the thermal annealing. We performed a series of experiments and found that the optimal settings for this method were *annealing for 5 hours at 375°C temperature*. Even though the number of thin flakes produced this way was larger than by mechanical exfoliation, the characterization with Raman spectroscopy revealed dramatic differences. For most of the cases studied, the bulk Raman active modes of GeSe at 150 cm^{-1} (B^1_{3g}) and 190 cm^{-1} (A^1_g) were replaced by two new vibrational modes with energies of 119 cm^{-1} and 213 cm^{-1}. Only on the very thick of our samples, we could see a co-existence of bulk GeSe modes and the new ones that appear because of the thermal annealing treatment. AFM analysis showed that even though thermal annealing produced thin flakes, it couldn't provide samples close to a mono- or bi-layer. These data combined with the drastic changes we found in the Raman spectra of thermally annealed flakes raise the question of what exactly happens to the GeSe crystal under the intense conditions of annealing.

To explain this behavior and evaluate thermal annealing as a suitable exfoliation method for GeSe crystal, our first thought was whether we oxidized our crystal during the experiment. The samples were for the most part 5 hours at 375°C in an oven, conditions that may lead to oxidation. In Fig.8.1, we summarize all the observed modes for several flakes with different thickness.

Thickness (nm)	Raman mode (cm^{-1})																	
	0	1	2	3	5	6	7	8	9	10	11	12	13	14	15	15	16 (broad)	17 (broad)
17		118.7	-	-	-	-	-	-	213.2	-	-	-	-	306.5	-	-	-	-
45	-	119.7	-	-	-	-	-	-	213.7	-	-	-	-	-	-	-	-	430
60	controversial sample due to laser thinning																	
80	controversial sample due to laser thinning																	
110	115.6	119.7	128.8	-	-	-	-	-	212.7	251.6	271.1	-	-	308.1	331.3	-	-	429
120	-	-	-	-	151.9	171.4	184.6	190.1	212.6	-	-	-	-	308	-	-	-	-
160	115.6	119.7	128.8	145.8	153.9	169.6	183.3	-	213.2	251.8	272.5	287.8	299.6	308	330.9	393.1	~423	429
250	-	119.2	128.8	-	153.4	-	183.8	187.1	212.7	251.8	272.5	287.8	298.9	307.7	330.9	391.7	~423	429
650	115.6	119.2	126.1	147.7	-	-	184.3	187.7	212.3	251.8	-	-	-	-	-	-	-	-
700	-	119.2	-	148.6	-	-	-	187.7	212.7	251.8	271.6	287.5	-	307.7	330.9	391.6	~423	-

Figure 8.1: Raman modes for several thermally annealed samples of different thickness. The thickness was determined by AFM measurements

The vibrational modes at 119 cm^{-1} and 213 cm^{-1} are present on all these samples. However, for samples thicker than 100 nm, these two modes co-exist with the bulk GeSe modes (B^1_{3g} and A^1_g). The main vibrational modes for the oxidized Ge, i.e. GeO_2, are at 168 cm^{-1}, 213 cm^{-1} and 443 cm^{-1}, with the last one to dominate the spectrum. But in our spectra this mode is completely absent. The argument for oxidation weakens even more if one compares the intensities of the 168 and 213 cm^{-1} modes. The intensity of the 168 cm^{-1} mode has to be almost 10 times the intensity of the 213cm^{-1} in case of oxidation. Clearly, this is not the case in our spectra where the 213 cm^{-1} is the dominant vibrational mode **[46-49]**.

Therefore, we should find a different approach to explain the results of thermal annealing. The next possible scenario is the phase transition of GeSe crystal to $GeSe_2$. In our spectra we see two sharp dominant modes at 119 cm^{-1} and 213 cm^{-1}, also present in $GeSe_2$ **[51]**. Therefore, it is very possible we may have a phase transition during thermal annealing to the more stable $GeSe_2$.

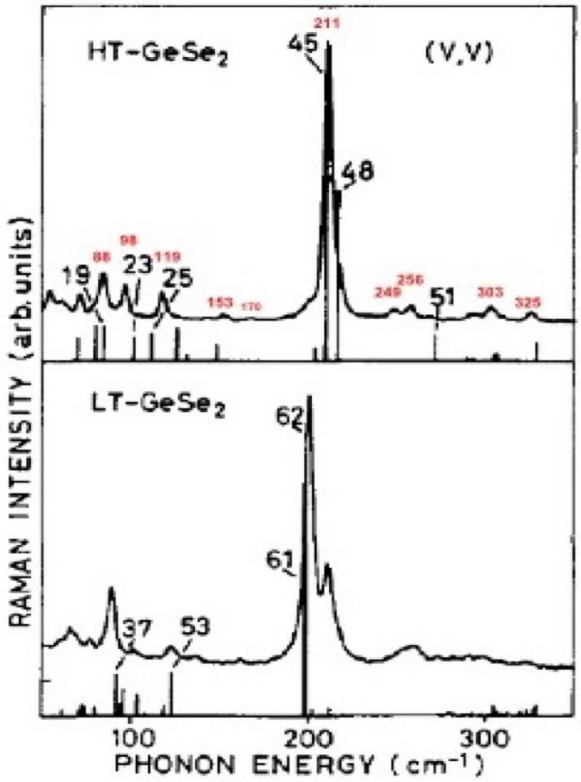

	HT-$GeSe_2$	GeSe thermally annealed
Raman Modes in cm^{-1}	88, 98, **119**, 153, 170, **211**, 249, 256, 303, 325	**119**, 154, 170, **213**, 251, 300, 308, 330

Figure 8.2: Raman spectral analysis of HT-$GeSe_2$ and LT-$GeSe_2$ from Inoue et al, SSC 79, 905 (1991).

Inoue et al., **[51]** have studied in detail the Raman vibrational modes of GeSe2 (Fig.8.2) and they have reported that the main vibrational mode is at 213 cm^{-1}. They also report the relative intensities of several modes and this way we could quantify our results. The intensity of the 213 mode is 10 times higher than that of the 119 cm^{-1} and also the 119 mode is 9 times stronger than the one at 153 cm^{-1}. These are the exact ratios we also measure (Fig.8.3). Therefore, we can safely argue that during annealing we are changing the GeSe to a more stable phase of $GeSe_2$.

	HT-$GeSe_2$	GeSe thermally annealed
I_{211}/I_{119} and I_{213}/I_{119}	10	10
I_{119}/I_{153} and I_{119}/I_{154}	9	9

Figure 8.3: Intensity ratios comparison for the Raman modes 211-213 cm^{-1} 119 cm^{-1} and 153-154 cm^{-1} between HT-$GeSe_2$ and thermally annealed GeSe

We also combined thermal annealing with laser thinning because during data acquisition we observed interesting changes caused by the laser of the Raman setup on our annealed flakes as function of time. The initial idea was to use a laser source on annealed flakes to reduce the thickness even further down (trying to reach single-layer flake) in a more controllable way since the laser energy is localized. The results after this series of experiments revealed differences in the Raman spectra. We manage to thin down our thermally annealed flakes even more by repeatedly use the 780nm laser while acquiring Raman spectra. We kept the intensity of the laser at the 10% level and repeated the experiment several times (Fig.8.4), in an accumulative time of 10 seconds, on the same flake **[52]**.

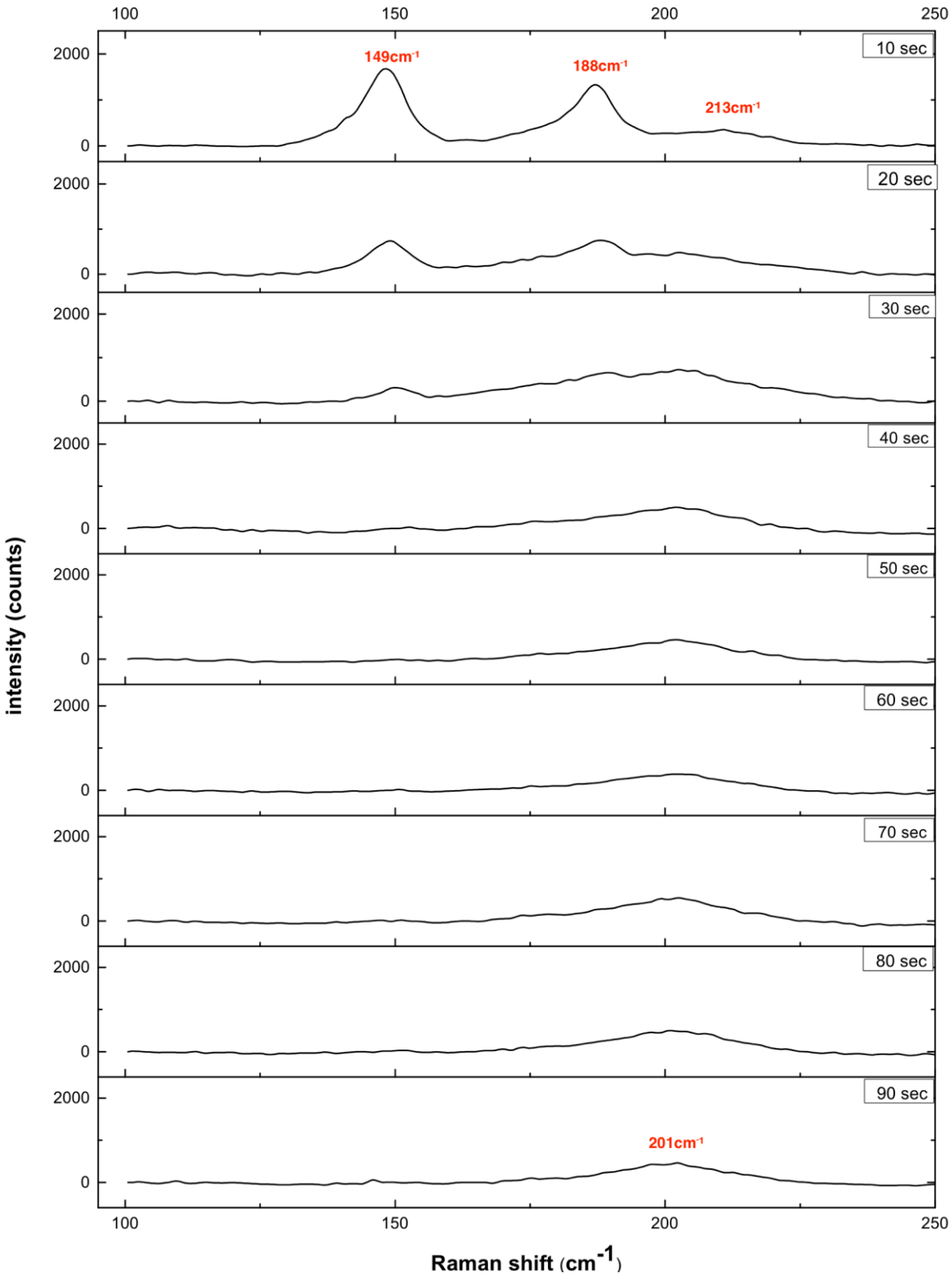

Figure 8.4: Evolution of Raman modes during laser thinning on annealed flake using 780nm wavelength (10%).

While initially we start with the bulk GeSe modes and the one at 213cm^{-1} mode, after almost one minute only one very broad mode at 201cm^{-1} remains. This mode agrees with Raman spectral analysis for LT-$GeSe_2$ and we conclude that while thermal annealing causes phase transition of GeSe crystal structure to $GeSe_2$, the combination with laser thinning leads to the creation of $GeSe_2$ in the amorphous state.

For the last part of our experiments, we revisited the initial goal which was to create and study thin flakes of GeSe crystal while evaluating exfoliation methods that could lead us to this direction. To this end, we tried to thin down GeSe flakes created by scotch tape exfoliation using the 473nm wavelength of the Raman setup. We chose a shorter wavelength this time because our targets weren't annealed and therefore it was harder to thin them down. With this experimental procedure we avoided phase transition and tried to directly create thinner flakes of GeSe.

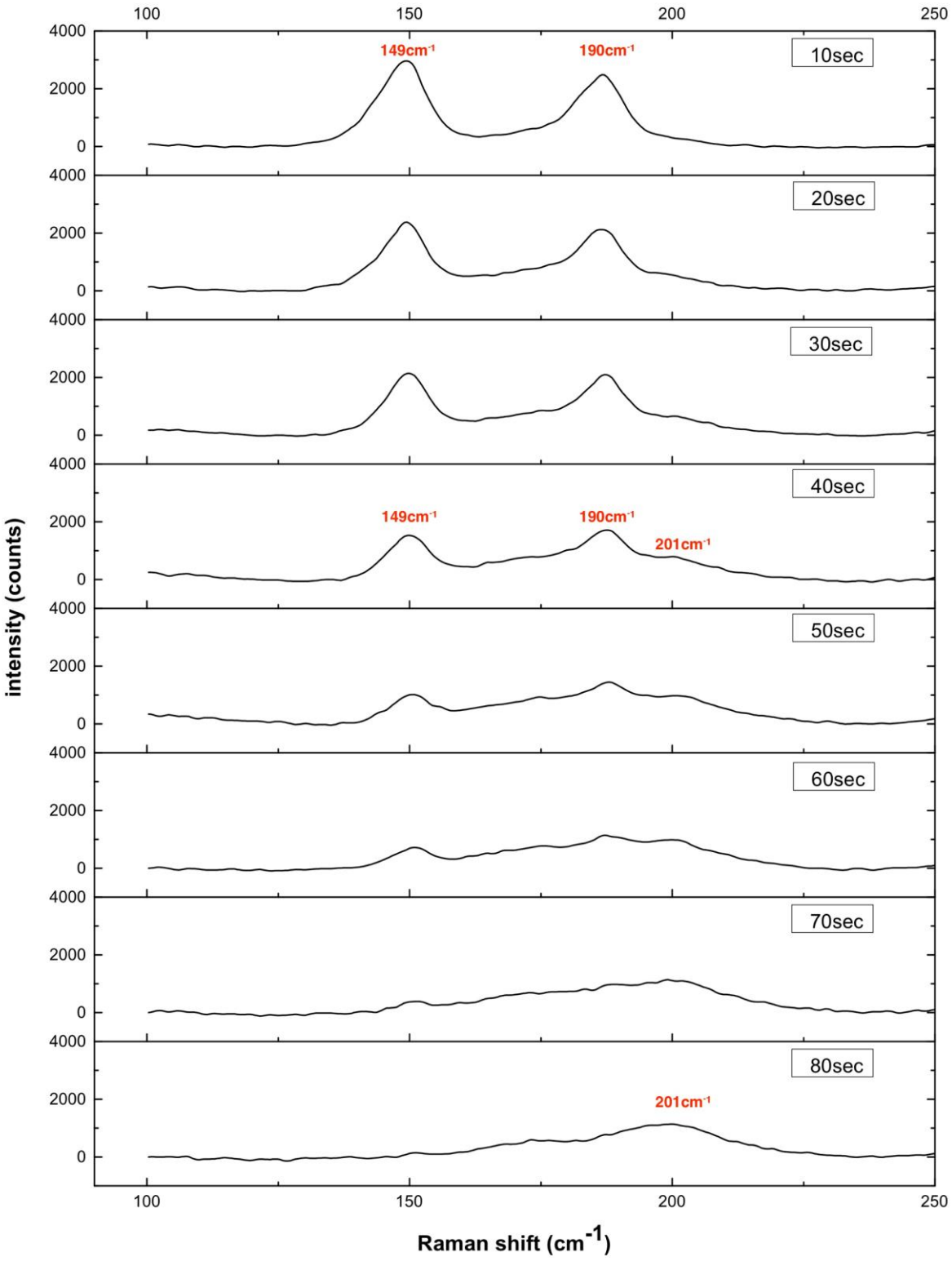

Figure 8.5: Evolution of Raman modes during laser thinning on GeSe flakes created by scotch-tape exfoliation using 473nm wavelength (100%).

The resulting spectral analysis revealed that we didn't encounter any phase transition to $GeSe_2$. However, the final spectra of both laser thinning experiments (for annealed and pristine flakes) ended up with the same remaining mode at 201cm^{-1} which corresponds to the amorphous GeSe.

Future work and perspectives

The series of experiments we performed to reach a single or double-layer structures, revealed how challenging is to create few-layers of GeSe that will still hold crystallinity and won't undergo any transition to another more stable state ($GeSe_2$). We have shown that performing conventional exfoliation techniques is not the right approach to isolate few layers of GeSe since the results weren't anywhere close to what we've seen for other materials like MoS_2 or Graphene. We might consider altering the conditions under which we apply any exfoliation to control better values like pressure and/or temperature evaluating this way whether it is possible to find the exact settings to reach single or double-layer GeSe. However, even though there is no report in the literature on CVD growth, in our opinion is the most promising way to achieve few GeSe layers in a controllable way.

References

1. Akinwande, D. et al. A review on mechanics and mechanical properties of 2D materials—Graphene and beyond. Extrem. Mech. Lett. 13, 42–77 (2017).
2. Mak, K. F. & Shan, J. Photonics and optoelectronics of 2D semiconductor transition metal dichalcogenides. Nat. Photonics 10, 216–226 (2016).
3. Grigorenko, A. N., Polini, M. & Novoselov, K. S. Graphene plasmonics. Nat. Photonics 6, 749–758 (2012).
4. Shiue, R. J. et al. Enhanced photodetection in graphene-integrated photonic crystal cavity. Appl. Phys. Lett. 103, (2013).
5. Gogotsi, Y. & Simon, P. True performance metrics in electrochemical energy storage. Science (80-.). 334, 917–918 (2011).
6. Mak, K. F., Lee, C., Hone, J., Shan, J. & Heinz, T. F. Atomically thin MoS2: A new direct-gap semiconductor. Phys. Rev. Lett. 105, 2–5 (2010).
7. Fei, R., Li, W., Li, J. & Yang, L. Giant piezoelectricity of monolayer group IV monochalcogenides: SnSe, SnS, GeSe, and GeS. Appl. Phys. Lett. 107, (2015).
8. Novoselov, K. S. et al. Two-dimensional atomic crystals. Proc. Natl. Acad. Sci. 102, 10451–10453 (2005).
9. Tongay, S. et al. Broad-range modulation of light emission in two-dimensional semiconductors by molecular physisorption gating. Nano Lett. 13, 2831–2836 (2013).
10. Shi, G. & Kioupakis, E. Anisotropic Spin Transport and Strong Visible-Light Absorbance in Few-Layer SnSe and GeSe. Nano Lett. 15, 6926–6931 (2015).
11. Taube, A., Łapińska, A., Judek, J., Wochtman, N. & Zdrojek, M. Temperature induced phonon behaviour in germanium selenide thin films probed by Raman spectroscopy. J. Phys. D. Appl. Phys. 49, (2016).

12. Gomes, L. C. & Carvalho, A. Phosphorene analogues: Isoelectronic two-dimensional group-IV monochalcogenides with orthorhombic structure. Phys. Rev. B - Condens. Matter Mater. Phys. 92, (2015).
13. A. Splendiani, et al. Emerging photoluminescence in monolayer MoS2. Nano Lett 10, 1271-1275 (2010).
14. T. Korn, Heydrich, S., Hirmer, M., Schmutzler, J. & Schüller, C. Low-temperature photocarrier dynamics in monolayer MoS2. Applied Physics Letters 99, 102109 (2011).
15. Q. H. Wang, , Kalantar-Zadeh, K., Kis, A., Coleman, J. N. & Strano, M. S. Electronics and optoelectronics of two-dimensional transition metal dichalcogenides. Nat Nanotechnol 7, 699-712 (2012).
16. M. Bernardi, Palummo, M. & Grossman, J. C. Extraordinary sunlight absorption and one nanometer thick photovoltaics using two-dimensional monolayer materials. Nano Lett 13, 3664-3670 (2013).
17. F. K. Perkins, A.L. Friedman, E. Cobas, P.M. Campell, G.G. Jernigan, and B.T. Jonker, Chemical vapor sensing with monolayer MoS2. Nano Lett 13, 668-673 (2013).
18. Radisavljevic, B., Radenovic, A., Brivio, J., Giacometti, V. & Kis, A. Single-layer MoS2 transistors. Nat Nanotechnol 6, 147-150 (2011).
19. Pospischil, A.; Furchi, M. M.; Mueller, T. Nat. Nanotechnol. 2014, 9, 257−261
20. Zhao, L.; Lo, S.; Zhang, Y.; Sun, H.; Tan, G.; Uher, C.; Wolverton, C.; Dravid, V. P.; Kanatzidis, M. G. Nature 2014, 508, 373−377
21. Shi, G.; Kioupakis, E. J. Appl. Phys. 2015, 117, 065103
22. Tritsaris, G. A.; Malone, B. D.; Kaxiras, E. J. Appl. Phys. 2013, 113, 233507
23. Singh, A. K.; Hennig, R. G. Appl. Phys. Lett. 2014, 105, 042103
24. M. Taniguchi et al., PRB42, 3634 (1990)
25. Hu, Y. et al. GeSe monolayer semiconductor with tunable direct band gap and small carrier effective mass. Appl. Phys. Lett. 107, (2015).

26. Gomes, L. C., Carvalho, A. & Castro Neto, A. H. Enhanced piezoelectricity and modified dielectric screening of two-dimensional group-IV monochalcogenides. Phys. Rev. B - Condens. Matter Mater. Phys. 92, 1–8 (2015).
27. Zhang, X. et al. Thermoelectric properties of GeSe. J. Mater. 2, 331–337 (2016).
28. Li, Z. et al. The electronic structure of GeSe monolayer with light nonmetallic elements decoration. Superlattices Microstruct. 109, 829–840 (2017).
29. Zhang, S. et al. Structural and electronic properties of atomically thin germanium selenide polymorphs. Sci. China Mater. 58, 929–935 (2015).
30. C. R. Rannewurf and R. J. Cashman, J. Phys. Chem. Solids Pergamon Press, 22, 293-298 (1961)
31. Kannewurf, C. R. & Cashman, R. J. Optical absorption and photoconductivity in germanium selenide. J. Phys. Chem. Solids 22, 293–298 (1961).
32. Mark Fox, Optical Properties of Solids, Oxford University Press, 2nd edition (2010), and M. Grundmann, The Physics of Semiconductors: An Introduction Including Devices and Nanophysics, Springer 2nd edition
33. C.V. Raman and K.S. Krishnan, Nature, A New Type of Secondary Radiation, 121, 501 (1928)
34. J. R Ferraro, K. Nakamoto and C. W. Brown, Introductory Raman Spectroscopy, Elsevier (2003)
35. E. Smith and G. Dent, Modern Raman Spectroscopy - A Practical Approach, John Wiley and sons, Ltd 2005
36. P. Yu, M. Cardona, Fundamentals of Semiconductors: Physics and Materials Properties, Springer, 2010 (Fourth edition), p. 396 – 397
37. Zhang, X., Tan, Q.-H., Wu, J.-B., Shi, W. & Tan, P.-H. Review on the Raman spectroscopy of different types of layered materials. Nanoscale 8, 6435–6450 (2016).

38. T.FukunagaS.SugaiT.KinosadaK.Murase, Observation of new Raman lines in GeSe and SnSe at low temperatures, Solid State Communications Volume 38, Issue 11, June 1981, Pages 1049-1052

39. H.R.ChandrasekharU.Zwick, Raman scattering and infrared reflectivity in GeSe, Solid State Communications Volume 18, Issues 11–12, May 1976, Pages 1509-1513

40. Popović, Z. V. et al. Raman scattering and infrared reflectivity in [(InP)5(In0.49Ga0.51As)8]30superlattices. J. Appl. Phys. 88, 6382–6387 (2000).

41. Nicolet Almega XR: High-Performance Dispersive Raman Spectrometers, Extracted from http://anff-q.org.au/wp-content/uploads/2016/07/Vibrational-Spectroscopy-Suite-Nicolet-Almega-XR-dispersive-Raman-microscope-brochure.pdf

42. Yi, M. & Shen, Z. A review on mechanical exfoliation for the scalable production of graphene. J. Mater. Chem. A 3, 11700–11715 (2015).

43. Wu, J. et al. Layer thinning and etching of mechanically exfoliated MoS2nanosheets by thermal annealing in air. Small 9, 3314–3319 (2013).

44. Huang, Y. et al. Reliable Exfoliation of Large-Area High-Quality Flakes of Graphene and Other Two-Dimensional Materials. ACS Nano 9, 10612–10620 (2015).

45. Castellanos-Gomez, A. et al. Laser-thinning of MoS2: On demand generation of a single-layer semiconductor. Nano Lett. 12, 3187–3192 (2012).

46. Liu, Y. et al. Layer-by-layer thinning of MoS2by plasma. ACS Nano 7, 4202–4209 (2013).

47. Micoulaut, M., Cormier, L. & Henderson, G. S. The structure of amorphous, crystalline and liquid GeO2. J. Phys. Condens. Matter 18, (2006).

48. Mernagh, T. P. & Liu, L. Temperature dependence of Raman spectra of the quartz- and rutile-types of GeO2. Phys. Chem. Miner. 24, 7–16 (1997).

49. Gillet, P., Le Cléac'h, A. & Madon, M. High-temperature raman spectroscopy of SiO 2 and GeO 2 Polymorphs: Anharmonicity and thermodynamic properties at high-temperatures. J. Geophys. Res. 95, 21635 (1990).

50. De Oliveira, I. S. S. & Longuinhos, R. Effects of oxygen contamination on monolayer GeSe: A computational study. Phys. Rev. B 94, 1–6 (2016).

51. Koichi Inoue, * Osamu Matsuda & Kazuo Murase, Raman Spectra Of Tetrahedral Vibrations In Crystalline Germanium Dichalcogenides, GeS_2 And $GeSe_2$ In High And Low Temperature Forms. Solid State Communications 79, 905–910 (1991).

52. Popović, Z. V. & Nikolić, P. M. Infrared and Raman spectra of GeSe2. Solid State Commun. 27, 561–565 (1978).

53. Jakšić, Z. M. Temperature and pressure dependence of phonon frequencies in GeS2, GeSe2, and SnGeS3. Phys. Status Solidi 239, 131–143 (2003)